Draft version February 6, 2022
Typeset using LaTeX **twocolumn** style in AASTeX63

arXiv:2105.12753v1 [astro-ph.GA] 26 May 2021

Extended X-ray emission associated with the radio lobes and the environments of 60 radio galaxies

Ajay Gill,[1,2] Michelle M. Boyce,[3] Christopher P. O'Dea,[3] Stefi A. Baum,[4] Preeti Kharb,[5] Neil Campbell,[6] Grant R. Tremblay,[7] and Suman Kundu[8]

[1] *David A. Dunlap Dept. of Astronomy and Astrophysics, University of Toronto, 50 St. George Street, Toronto, ON, Canada M5S 3H4*
[2] *Dunlap Institute for Astronomy and Astrophysics, University of Toronto, 50 St. George Street, Toronto, ON, Canada M5S 3H4*
[3] *Department of Physics and Astronomy, University of Manitoba, Winnipeg, MB R3T 2N2, Canada*
[4] *Faculty of Science, University of Manitoba, Winnipeg, MB R3T 2N2, Canada*
[5] *National Centre for Radio Astrophysics, TIFR, Post Bag 3, Ganeshkhind, Pune 411007, India*
[6] *Physics Department, 2320 Chamberlin Hall, University of Wisconsin-Madison,1150 University Avenue, Madison, Wisconsin 53706, USA*
[7] *Harvard-Smithsonian Center for Astrophysics, 60 Garden St., Cambridge, MA 02138, USA*
[8] *Centre for Nano and Soft Matter Sciences, P.B.No.1329, Prof UR Rao Road, Jalahalli, Bengaluru, 560013, India*

ABSTRACT

This paper studied the faint, diffuse extended X-ray emission associated with the radio lobes and the hot gas in the intracluster medium (ICM) environment for a sample of radio galaxies. We used shallow ($\sim$ 10 ks) archival *Chandra* observations for 60 radio galaxies (7 FR I and 53 FR II) with $0.0222 \leq z \leq 1.785$ selected from the 298 extragalactic radio sources identified in the 3CR catalog. We used Bayesian statistics to look for any asymmetry in the extended X-ray emission between regions that contain the radio lobes and regions that contain the hot gas in the ICM. In the *Chandra* broad band ($0.5-7.0$ keV), which has the highest detected X-ray flux and the highest signal-to-noise ratio, we found that the non-thermal X-ray emission from the radio lobes dominates the thermal X-ray emission from the environment for $\sim 77\%$ of the sources in our sample. We also found that the relative amount of on-jet axis non-thermal emission from the radio lobes tends to increase with redshift compared to the off-jet axis thermal emission from the environment. This suggests that the dominant X-ray mechanism for the non-thermal X-ray emission in the radio lobes is due to the inverse Compton upscattering of cosmic microwave background (CMB) seed photons by relativistic electrons in the radio lobes, a process for which the observed flux is roughly redshift independent due to the increasing CMB energy density with increasing redshift.

Keywords: thermal bremsstrahlung emission, inverse Compton scattering, active radio galaxies

1. INTRODUCTION

Radio galaxies provide a number of important challenges to astrophysics, including those of jet launching, propagation, and effects on the host galaxy and environment (see e.g. Heckman & Best 2014; Padovani 2016; Tadhunter 2016; Padovani et al. 2017; Blandford et al. 2019; Hardcastle & Croston 2020). The dominant emission mechanism in the radio wavelengths is synchrotron emission, where radiation is emitted by relativistic electrons gyrating through magnetic fields. Synchrotron emission is non-thermal in origin and is typically parameterized by a power law of the form $S_\nu \propto \nu^{-\alpha}$, where S_ν is the flux density, ν is the frequency, and α is the spectral index.

Fanaroff & Riley (1974) suggested that radio galaxies could be categorized into two general luminosity/morphology classes, namely FR I and FR II. For FR I (FR II) sources, the ratio of the distance between the brightest spots of radio emission on either side of the center to the full extent of the source is less (greater) than 0.5. The FR II sources tend to have higher radio powers ($> 10^{25}$ W Hz^{-1}) than the FR Is. The FR types also separate in the radio luminosity versus optical host galaxy luminosity plane (see e.g. Ledlow & Owen 1996; Buttiglione et al. 2010). Detailed discussions of the differences between FR I and FR II are given by e.g., Bridle (1984) and Baum et al. (1995).

X-ray observations provide for a near complete detection of active galactic nuclei (AGNs) with minimal contamination from non-AGN sources (Padovani et al. 2017). The reasons for this are: (i) X-ray emission from AGN seems to be nearly universal; (ii) X-rays can penetrate through high column densities of gas and dust; and (iii) X-ray emission from host galaxy astrophysical processes are typically weak compared to the AGN (Brandt & Alexander 2015). Radio galaxies consist of a compact core at the nucleus, extended radio lobes, hotspots, and collimated radio jets, all of which may radiate X-ray emission (see e.g. Massaro et al. 2015a; Mingo et al. 2017; de Vries et al. 2018; Massaro et al. 2018).

Several emission mechanisms have been proposed for the X-ray emission from radio galaxies (see e.g. Harris & Krawczynski 2002; Harris & Krawczynski 2006). Thermal bremsstrahlung emission does not provide a satisfactory model for the X-ray emission associated with radio lobes and hotspots because (i) the required amount of hot gas is large ($\sim 10^{10}$ $M_{\odot}$), (ii) the gas needs to be far from the host galaxy, and (iii) the predicted Faraday rotation and depolarization are not observed (Harris & Krawczynski 2002). The bright compact hotspots at the end of jets can be consistent with either synchrotron or synchrotron self Compton (SSC) emission (Harris et al. 1994; Hardcastle et al. 2004; Mingo et al. 2017). In the diffuse radio lobes, the dominant photon field is the Cosmic Microwave Background (CMB) (e.g., Croston et al. 2005), and inverse Compton (IC) scattering of the CMB photons by relativistic electrons has been found to be consistent with X-ray observations of the radio lobes (see e.g. Tavecchio et al. 2000; Celotti et al. 2001; Harris & Krawczynski 2002; Croston et al. 2005; Kharb et al. 2012a; Stanley et al. 2015; Ineson et al. 2017; Mingo et al. 2017).

For the low-luminosity FR I radio sources, the dominant extended emission mechanism in X-ray, optical, and radio from the jets is thought to be due to the synchrotron process (e.g., Sambruna et al. 2004; Worrall 2009; Kharb et al. 2012b). This is supported by the intrinsic variability found in the knots of the M87 jet (Harris et al. 2006), and the fact that in most cases the X-ray spectral index α_x is greater than 1 and much greater than the radio spectral index α_r, as well as the relative morphologies in the X-ray, optical, and radio.

The purpose of this study was to search for faint, diffuse extended X-ray emission associated with the radio lobes and the hot gas in the intracluster medium (ICM) environments for a sample of 60 radio galaxies observed in shallow ($\sim$ 10 ks) archival *Chandra* observations. Since the exposure times for the *Chandra* observations of the sources in our sample were short, detailed spectral modeling of the extended emission from the radio lobes and the environments was not possible. Instead, we studied the properties of the thermal and non-thermal extended emission of the sources in our sample by considering the spatial distribution of the emission. We did this by comparing the X-ray emission in regions that contain the radio lobes and regions that do not contain the radio lobes in the hot ICM environments. Our technique (described in §4) allows us to search for faint, diffuse X-ray emission. We might expect to see asymmetry in the diffuse X-ray emission, since as discussed above, there has been previous detection of non-thermal emission (synchrotron, SSC, or IC/CMB) associated with the radio plasma. Furthermore, the radio source itself can also influence the ambient thermal gas in the intergalactic and intracluster medium, forming bubbles/cavities in the ICM (see e.g. Rafferty et al. 2006; McNamara & Nulsen 2007; Cavagnolo et al. 2010; O'Sullivan et al. 2011; Hlavacek-Larrondo et al. 2012).

This paper is organized as follows. In §2, we present the sample selection criteria. The overview of the X-ray and radio data used in this study is presented in §3. The archival data analysis is described in §4, consisting of the data reduction procedure (§4.1), the quadrant selection and the point source blanking procedure (§4.2), the sky background estimation (§4.3), and the calculation of the X-ray emission asymmetry (§4.4). The results and the discussion are presented in §5 and §6, respectively. During this study, we found some sources with X-ray emission spatially correlated with the radio hotspots. These sources were not included in our sample and are instead reported in §7. In Appendix §A, we present the analytical framework for the Bayesian analysis used to compute the "ON/OFF jet-axis asymmetry" parameter, R (see Equation 1 in §4.4). In Appendix §B, we present the R values for each source by band. In Appendix §C, we present the properties of the science aperture as well as the X-ray and radio data for each source. Throughout this paper, we assume $H_0 = 72$ km s^{-1} Mpc^{-1}, $\Omega_{\rm M} = 0.27$, $\Omega_{\Lambda} = 0.73$, consistent with Dunkley et al. (2009).

2. SAMPLE SELECTION CRITERIA

The Third Cambridge catalog (3C) of 471 bright radio sources observed at 159 MHz was first published in 1959 (Edge et al. 1959). The 3C catalog was revised (3CR) in 1962 with observations at 178 MHz (Bennett 1962). The 3CR catalog has a flux limit of 9 Jy at 178 MHz and covers the entire northern hemisphere north of -5° in declination and contains 328 radio sources. In 1985, Spinrad et al. (1985) provided an update to the 3CR catalog with revised positions, redshifts, magnitudes, and identifications, and presented a list of 298 extragalactic radio sources, which forms the initial sample for this study. These 298 extragalactic sources form a heterogeneous sample in redshift and source type.

We selected 3CR sources which have *Chandra* X-ray data and have Very Large Array (VLA) radio data that shows the radio lobes and have a "science" aperture (see §4.2) that does not exceed the boundaries of the *Chandra* ACIS chip. We excluded three sources whose radio structure extended beyond the defined on-axis quadrants (see §4.2). Since the purpose of this study was to search for faint, diffuse extended X-ray emission associated with the radio lobes and the hot gas in the environment, we excluded sources with bright previously detected features as determined by visual inspection of the sources for bright X-ray jets or hotspots, as well as by using the XJET[1] catalog as a guide. Our final sample consists of 60 sources (7 FR I and 53 FR II). The redshift distribution of the sample is shown in Figure 1, and is between $0.0222 \leq z \leq 1.785$.

[1] `https://hea-www.harvard.edu/XJET/`

3. X-RAY AND RADIO DATA

We used archival *Chandra* (Weisskopf et al. 2002) observations for the radio sources in our sample. The low background levels, high angular resolution, and the collecting area of *Chandra* allows it to detect sources three orders of magnitude fainter than previous generation X-ray observatories. The radio images for the sources in our sample consisted of images observed with the VLA retrieved from the NRAO Science Data Archive[2] as well as from colleagues. L-band ($1.0-2.0$ GHz) radio images were preferentially used due to their superior detection of the radio lobes. Higher frequency C-band ($4.0-8.0$ GHz) and X-band ($8.0-12.0$ GHz) images were used when L-band images for a particular source were unavailable. The archival *Chandra* data is mostly from the snapshot observations of Massaro and collaborators (Massaro et al. 2012, 2013, 2015b, 2018) with exposure times of ~ 10 ks. The FR classifications of the sources in our final sample were taken from Massaro et al. (2015a).

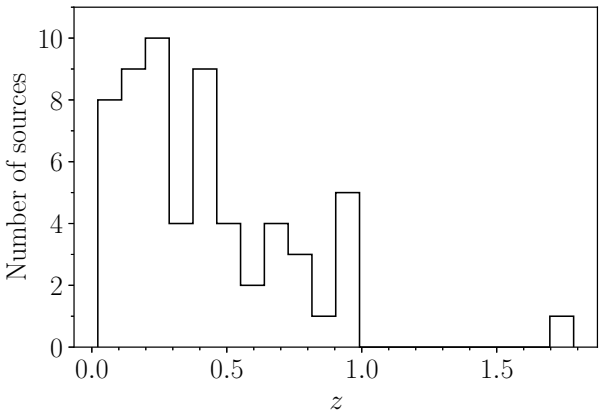


Figure 1. Redshift distribution of the sample in this study, consisting of 60 extragalactic radio sources (7 FR I and 53 FR II) with redshifts between $0.0222 \leq z \leq 1.785$ selected from the 298 extragalactic radio sources from the 3CR catalog (Bennett 1962).

4. ARCHIVAL DATA ANALYSIS

4.1. *Data Reduction Procedure*

The X-ray event files of the sources in our sample were taken from the *Chandra* ChaSeR data archive.[3] The *Chandra* datasets are listed in Table 4.

A circular science aperture consisting of four quadrants of equal area was overlaid on the source to determine the extended X-ray emission asymmetry between regions containing the radio lobes and those that do not. We considered four different X-ray energy bands defined by the *Chandra* ACIS Science Energy Bands[4] with effective energies: soft ($0.5-1.2$ keV), medium ($1.2-2.0$ keV), hard ($2.0-7.0$ keV), and broad ($0.5-7.0$ keV).

The *Chandra* data were reduced following the standard procedure described in the *Chandra Interactive Analysis of Observations* (CIAO) threads,[5] using CIAO version 4.8 and *Chandra Calibration Database* version CALDB version 4.7.2. The `chandra_repro` command was used to process the data from the standard data distribution. The parameters `destreak`, `badpixel`, and `process_events` were used to detect streak events and create a bad pixel and level 2 event file.

For sources with multiple observations, `reproject_obs` was used to reproject the observations to a common tangent point. The native ACIS pixel size is $0.492''$. A binning factor of 0.5 corresponding to $0.246''$ per pixel was used to adequately sample the point spread function. Four exposure-corrected images were created using the `flux_obs` command for the soft, medium, hard, and broad bands, where the intensity level in each pixel was in units of counts s^{-1}.

4.2. *Quadrant selection and point source blanking procedure*

For each source in our sample, the radio image was used as a reference to construct a circular "science" aperture with four quadrants of equal area. Two quadrants were on-axis (each containing a radio lobe), and the other two quadrants were off-axis (each not containing a radio lobe). The radius of the aperture was manually chosen by visual inspection for each individual source by careful consideration of the extent of the radio lobes seen in the selected radio images, such that both radio lobes are sufficiently contained within the aperture (see Figure 2). The science apertures are also given in Table 4 and the counts in the apertures are given in Table 5. Three sources (3C 76.1, 3C 288, and 3C 433) which had radio structure that extended beyond the nominal on-axis quadrants were excluded from the analysis. The science aperture was then overlaid onto the exposure-corrected X-ray image of the source. The broadband *Chandra* image was used for selecting the center of the science aperture, since it contains the widest energy range of all bands and hence the highest signal-to-noise ratio.

We note that about 97% of 3CR radio nuclei are detected in short observations by *Chandra* (Massaro et al. 2012, 2013, 2015b, 2018). Thus, it was relatively simple to overlay the science aperture (determined from the radio image) onto the *Chandra* image and center it on the X-ray nucleus. Any miscentering of a few pixels between the radio and X-ray core should not affect the on-jet and off-jet axis counts, since (i) the X-ray nucleus region is blanked, and (ii) the extent and area of the radio lobes

[2] `https://archive.nrao.edu/archive/`

[3] `http://cda.harvard.edu/chaser/`

[4] `http://cxc.harvard.edu/csc/columns/ebands.html`

[5] `http://cxc.harvard.edu/ciao/guides/index.html`

and hence the quadrants is much larger than the X-ray nucleus. Therefore, a more sophisticated centroiding algorithm was not necessary for this study.

After the science aperture was constructed, the pixels of the point source at the nucleus were replaced with new values that were the mean of the Poisson distribution of pixel values in the background diffuse emission. This was done to remove unwanted nuclear emission from the quadrants, since the aim of the study was to investigate the asymmetry in only the diffuse extended X-ray emission between the on and off-axis radio lobe quadrants.

The `dmfilth` tool was used to fill the nuclear pixels with the background diffuse emission pixels, after which the `dmimgcalc` tool was used to obtain an exposure-corrected X-ray image, which we call the "blanked" image. The radius of the exclusion circle used for blanking the point source at the nucleus was manually selected by visual inspection of (i) the overdensity of bright pixels associated with the X-ray nucleus in the broadband image, and (ii) comparison to the radio core. This radius varied for each source, and was typically between 2.5 to 5 arcseconds. For the `dmfilth` tool, the background region was an annulus around the exclusion region. The radius of the background region was chosen to be three times larger than the radius of the exclusion region, with a gap between the exclusion region and background region of 0.5 pixels to ensure there is sufficient separation between the inner radius of the background region and the exclusion region.

To test whether choosing a larger background radius has any affect on the ON−OFF axis counts, we looked at the source 3C 401 as a test source and used a background radius that is ten times larger than the exclusion radius. We found no difference in the ON−OFF axis ratio between the cases whether the radius is three times larger or ten times larger than the exclusion region. Therefore, a background region with a three times larger radius than the exclusion region should be sufficient for the purpose of blanking the nucleus in this study. The blanking procedure we followed is described in further detail in *An Image of Diffuse Emission* in the *CIAO 4.9 Science Threads*.[6] Figure 2 shows an example of the quadrant selection and point source blanking procedure with the unblanked and blanked image of 3C 401.

4.3. *Background Estimation*

After the X-ray data were reduced and the point source blanking was complete, the image was also background subtracted. The background level was estimated by constructing between one and three circular "background" apertures with the same radius as the science aperture. The background apertures were placed away from the science aperture in the background regions

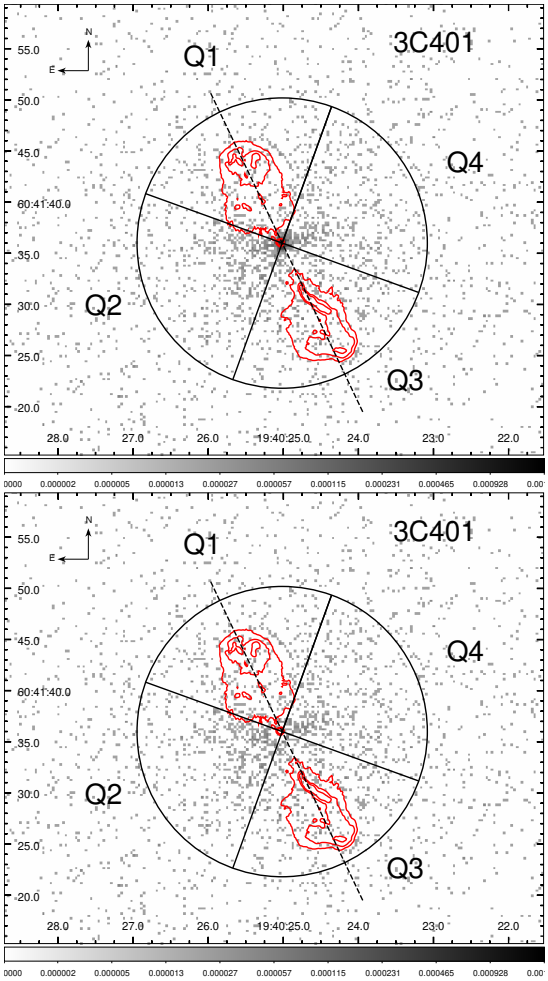


Figure 2. 3C 401 X-ray broadband (0.5 − 7.0 keV) image before (top) and after (bottom) blanking. X-ray emission: gray pixels. Radio emission: red contours. The X-ray data consists of a combination of two observations (with *Chandra* IDs 3083 and 4370) with exposure times of 22.66 ks and 24.85 ks, respectively. The radio image is an *X*-band VLA image.

(containing no point sources), while still being on the same ACIS chip as the science aperture. The background counts were estimated by summing the total number of counts in each background aperture and then taking the median of the three sums from the three apertures. We denote these median background counts for an aperture the size of the science aperture as B. We used the median of up to three apertures to estimate the background so that the background estimate is less biased toward the potential variability of the efficiency of the pixels across the ACIS chip. Three background apertures were preferentially used whenever possible. For a few sources, the science aperture was sufficiently large on the ACIS chip that it was only possible to construct only one or two background apertures. The background counts are given in Table 5.

[6] `http://cxc.harvard.edu/ciao/threads/diffuse_emission/`

4.4. *Calculation of the X-Ray Emission Asymmetry*

The ON−OFF jet-axis asymmetry is calculated as

$$R = \frac{S_{\rm ON} - S_{\rm OFF}}{(S_{\rm ON} + S_{\rm OFF})\,/\,2}\,, \tag{1}$$

where

$$\left.\begin{aligned} S_{\rm ON} &= {\rm Counts}_{\rm Q1} + {\rm Counts}_{\rm Q3} \\ S_{\rm OFF} &= {\rm Counts}_{\rm Q2} + {\rm Counts}_{\rm Q4} \end{aligned}\right\} \tag{2}$$

such that $R > 0$ means more on-axis emission, $R = 0$ means symmetric emission, and $R < 0$ means more off-axis emission. The background counts are taken into consideration by

$$B_{\rm ON} = B_{\rm OFF} \equiv B/\,r \tag{3}$$

where $r = 2$,[7] and B is the estimated background counts within a background aperture with the same radius as the science aperture on the ACIS chip. As the X-ray data for the sources in our sample consist of relatively low counts, background subtraction must be done carefully to avoid negative values. As such, traditional error propagation techniques do not generally apply.

The approach taken here is to model Equation (1) using Bayesian analysis, as prescribed by Park et al. (2006) and van Dyk et al. (2001). The posterior distribution of R, given prior information $S_{\rm ON}$, $S_{\rm OFF}$, and B, is given by

$$\begin{aligned} P(R|S_{\rm ON}, S_{\rm OFF}, B) = &\sum_{i=0}^{S_{\rm ON}} \sum_{j=0}^{S_{\rm OFF}} \kappa_{ij}(S_{\rm ON}, S_{\rm OFF}, B, R) \\ &\times \frac{\Gamma(i + j + S_{\rm ON} + S_{\rm OFF} + 2)}{4^{i+j+S_{\rm ON}+S_{\rm OFF}+2}}\,, \end{aligned} \tag{4}$$

where

$$\begin{aligned} \kappa_{ij}(S_{\rm ON}, S_{\rm OFF}, B, R) = &\, N(i, S_{\rm ON}, B)\, N(j, S_{\rm OFF}, B) \\ &\times \left(1 + \frac{R}{2}\right)^{i+S_{\rm ON}} \left(1 - \frac{R}{2}\right)^{j+S_{\rm OFF}}\,, \end{aligned}$$

and

$$N(\ell, S_x, B) = \frac{\dfrac{\Gamma(S_x - \ell + 2B + 1)}{\Gamma(\ell + 1)\Gamma(S_x - \ell + 1)4^{S_x-\ell+2B+1}}}{\displaystyle\sum_{k=0}^{S_x} \frac{\Gamma(S_x - k + 2B + 1)\Gamma(k + S_x + 1)}{\Gamma(k + 1)\Gamma(S_x - k + 1)4^{S_x-k+2B+1}2^{k+S_x+1}}}\,,$$

[7] See Appendix A.

with x = ON, OFF, $\ell = i, j$, and $-2 \le R \le 2$, as derived in Appendix A. This formula allows us to simultaneously handle small (Poissonian) and large (Gaussian) statistics.

Figure 3 shows an example of the R distribution for source 3C 401 in the broad band, depicted in Figure 2. Figure 3 is consistent with the extended X-ray emission being off the jet-axis, i.e., $R_{\rm broad} = -0.17\pm\ 0.04$. Note that this particular example has rather high counts, $S_{\rm ON} = 777$ and $S_{\rm OFF} = 919$, with relatively low background, $B = 47$. The 68.27% ($\sim \pm 1\sigma$) Highest Posterior Density (HPD) region is also symmetrical about its mode. All implying, that Gaussian error propagation should apply: i.e.,

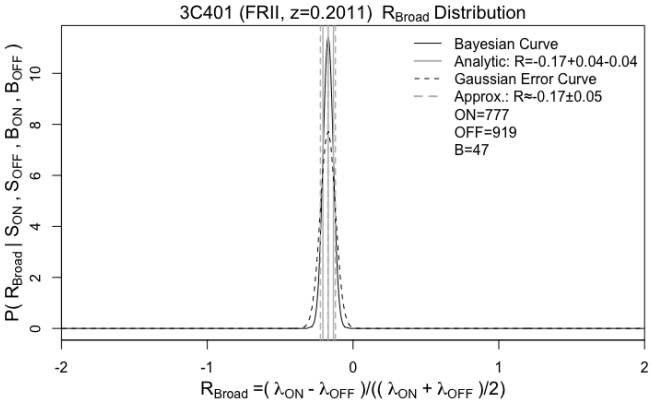


Figure 3. Posterior distribution of $R_{\rm broad}$ for 3C 401 of Figure 2, with mode −0.17 and a 68.27% Highest Posterior Density (HPD) region (Hoff 2010) of [−0.21, −0.13], i.e., $R_{\rm broad} = -0.17\pm\ 0.04$. So the X-ray emission is off the jet-axis.

$$R \simeq \frac{S_{\rm ON} - S_{\rm OFF}}{\dfrac{1}{2}\left(S_{\rm ON} + S_{\rm OFF} - 2\dfrac{B}{r}\right)} \pm \sigma_R \tag{5}$$

with error,

$$\sigma_R = \frac{\sqrt{\left(S_{\rm OFF} - \dfrac{B}{r}\right)^2 \sigma^2_{S_{\rm ON}} + \left(S_{\rm ON} - \dfrac{B}{r}\right)^2 \sigma^2_{S_{\rm OFF}} + \dfrac{\sigma^2_B}{r^2}}}{\dfrac{1}{4}\left(S_{\rm ON} + S_{\rm OFF} - 2\dfrac{B}{r}\right)^2}$$

where

$$\sigma_N \approx \sqrt{N + 0.75} + 1$$

for counts $N = S_{\rm ON}$, $S_{\rm OFF}$, B (Gehrels 1986). Plugging in the numbers, we find $R_{\rm broad} \simeq -0.17 \pm 0.05$ which is consistent with the analytical expression, Equation (4).

For low statistics, however, the approximation deviates significantly. Figure 4 shows an example of the R distribution for source 3C 22, in the soft band, where $S_{\rm ON} = 10$, $S_{\rm OFF} = 2$, and $B = 2$. Here the analyt-

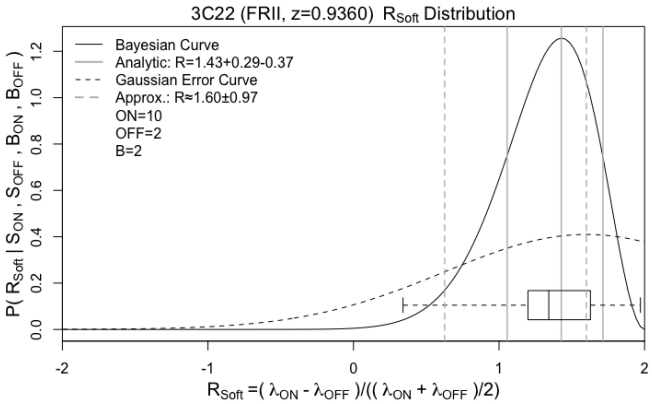


Figure 4. Posterior distribution of $R_{\rm soft}$ for 3C 22, with $R_{\rm soft} = 1.43^{+0.29}_{-0.37}$ for the analytic solution, and $R_{\rm soft} \simeq 1.60 \pm 0.97$ for the approximate method. Overlaid on the analytic curve is a box plot, with 99.3% HPD whiskers, 50% HPD box, and 1.34 median, providing a 1D method of visualizing a skewed 2D distribution (Hoff 2010): see Figure 5. So the X-ray emission is on the jet-axis.

ical expression, Equation (4), yields $R_{\rm soft} = 1.43^{+0.29}_{-0.37}$, whereas the approximation, Equation (5), yields $R_{\rm soft} \simeq 1.60 \pm 0.97$. A more detailed discussion on this subject can be found in Park et al. (2006).

For simplicity, $R \pm 1\hat{\sigma}$ shall be taken as shorthand for $R^{+\sigma_2}_{-\sigma_1}$, such that, $R - \sigma_1$ and $R + \sigma_2$ represent the lower and upper 68.27% HPD ($\sim \pm 1\sigma$) bounds, respectively, where R is the mode of the distribution function. This definition is convenient, as it is synonymous for either the analytic or approximate expression, Equations (4) or (5), respectively. Unless explicitly stated otherwise, we shall assume R is the mode of the distribution with $\pm 1\hat{\sigma}$ confidence intervals.

5. RESULTS

Table 3 (in Appendix B) shows the $R \pm 1\hat{\sigma}$ values obtained from Equations 4 and 5. Table 3 also includes redshift information. Table 4 (in Appendix C) shows the properties of the science aperture and the X-ray and radio data for each source. Table 5 shows the on-axis, off-axis and background counts.

Figure 5 shows the box plots of the median R values for the different bands with the results sorted by FR type and redshift for the sources in our sample, using the aforementioned information. This figure provides an overall birds-eye view of the R distribution functions, their skewness, and behavior with z. As noted in §4.4, the distributions become more Gaussian-like (less skewed) with increasing counts, as is evident when comparing with Table 5. This is particularly evident in the broad band, which has the highest counts.

Figure 6 shows the histograms of the R distributions for different bands. This is essentially a projection of the distribution functions of Figure 5, collapsed along z: i.e., no correlation is assumed. Here, the skewness represents a general broadening of the R-distributions about zero, with small $|R| > 0$ outlier-peaks. The broad band gives the overall average trend in R, from which we can ascertain, a slight ON-bias in the soft, medium bands, and broad bands, and a possible slight OFF-bias in the hard band. Figure 7 provides summary violin plots of the R values from Figure 6. The latter two figures emphasize the overall trend of the R distribution functions. Again, there is a general trend favoring $R > 0$ for the soft, medium, and broad bands, and $R < 0$ for the hard band. Table 1 provides a summary of median R values, within the 1st and 3rd quartile bounds, quantifying this trend.

Table 1. The median R values from Figure 7 with minus 25th (Q1) and plus 75th (Q3) percentile bounds.

Band	$R_{\rm combined}$	$R_{\rm FRI}$	$R_{\rm FRII}$
Soft	$+0.23^{+0.32}_{-0.24}$	$+0.09^{+0.19}_{-0.13}$	$+0.25^{+0.32}_{-0.24}$
Medium	$+0.33^{+0.32}_{-0.32}$	$+0.17^{+0.19}_{-0.16}$	$+0.36^{+0.32}_{-0.35}$
Hard	$-0.12^{+0.16}_{-0.21}$	$-0.17^{+0.11}_{-0.08}$	$-0.09^{+0.16}_{-0.24}$
Broad	$+0.23^{+0.16}_{-0.13}$	$+0.17^{+0.08}_{-0.05}$	$+0.23^{+0.19}_{-0.16}$

Table 2 shows the fraction of sources in the sample for which $R > 0$ or $R < 0$, within 68.27% HPD ($\pm 1\hat{\sigma}$), extracted from Table 3. Table 2 represents a fraction of the sample for which R is statistically different from symmetric emission in the on-jet and the off-jet regions.

Figure 8 shows R as a function of redshift for all the sources in our sample. Figure 9 shows $\overline{R}$ as a function of redshift in two redshift bins: (i) $0 < z < 0.5$ and (ii) $0.5 < z < 1.0$. $\overline{R}$ is the average of the R values for all sources in that particular redshift bin, and the error bars on $\overline{R}$ are the $\pm 1\hat{\sigma}$ error bars of all the sources in that particular redshift bin added in quadrature.

Figure 10 shows R as a function of radio power, respectively. The radio powers were calculated for the sources in our sample that have known 178 MHz fluxes taken from the 3CRR Extragalactic Database.[8] The radio power was calculated as

$$L_{\rm radio} = F_{178\,\rm MHz} \times 4\pi D_{\rm L}^2 \times (1+z)^{-(1+\alpha)} \qquad (6)$$

where $L_{\rm radio}$ is in units of W Hz^{-1}, $F_{178\,\rm MHz}$ is the flux density at 178 MHz in units of Jansky or erg s^{-1} cm^{-1} Hz^{-1}, $D_{\rm L}$ is the luminosity distance, and we used a power law index, $\alpha = -0.7$.

6. DISCUSSION

The broad band (0.5 − 7.0 keV) has the highest detected flux (and therefore the highest signal-to-noise ra-

[8] https://3crr.extragalactic.info/cgi/database

Table 2. Fraction of sources in our sample for which $R > 0$ or $R < 0$, within 68.27% HPD ($\pm 1\hat{\sigma}$).

Band	$N_{\rm both}(R \pm 1\hat{\sigma} > 0)$	$N_{\rm both}(R \pm 1\hat{\sigma} < 0)$	$N_{\rm FRI}(R \pm 1\hat{\sigma} > 0)$	$N_{\rm FRI}(R \pm 1\hat{\sigma} < 0)$	$N_{\rm FRII}(R \pm 1\hat{\sigma} > 0)$	$N_{\rm FRII}(R \pm 1\hat{\sigma} < 0)$
Soft	31/60 (51.7%)	5/60 (8.3%)	3/7 (42.9%)	0/7 (0.0%)	28/53 (52.8%)	5/53 (9.4%)
Medium	36/60 (60.0%)	6/60 (10.0%)	3/7 (42.9%)	0/7 (0.0%)	33/53 (62.3%)	6/53 (11.3%)
Hard	6/60 (10.0%)	24/60 (40.0%)	0/7 (0.0%)	4/7 (57.1%)	6/53 (11.3%)	20/53 (37.7%)
Broad	46/60 (76.7%)	3/60 (5.0%)	7/7 (100.0%)	0/7 (0.0%)	39/53 (73.6%)	3/53 (5.7%)

tio and the lowest error bars in R), so we focus on the broad band results for the physical interpretation. Table 2 shows that a majority ($\sim 77\%$) of the sources in our combined FR I and FR II sample have $R \pm 1\hat{\sigma} > 0$ in the broad band, suggesting that the non-thermal X-ray emission from the radio lobes typically dominates the thermal X-ray emission from the hot gas in the environments. On the other hand, the thermal emission from the ICM dominates the non-thermal emission from the lobes for only 5% of the sources in our combined sample.

For the FR I (FR II) subsample, the on-jet axis non-thermal emission dominates the off-jet axis thermal emission for 100% ($\sim 74\%$) of the sources, whereas the off-axis thermal emission dominates for 0% ($\sim 6\%$) of the sources.

The flux due to thermal bremsstrahlung emission from the hot gas in the off-jet axis regions in the ICM environments of radio galaxies can be expected to decrease with increasing redshift. On the other hand, the flux due to the IC scattering of the CMB photons by relativistic electrons in the radio lobes in the on-jet axis regions is roughly redshift independent due to the increasing CMB energy density with increasing redshift.

Figures 8 and 9 show that R tends to increase with redshift in the broad band. This marginal increase is also seen between R and the radio power, which can be expected since (i) radio power depends on redshift (see equation 6), and (ii) the selection function of the 3CR catalog, for which the 9 Jy flux density limit at $z = 1$ corresponds to a power of $\sim 4 \times 10^{28}$ W Hz^{-1}. The marginal increase in R with redshift is consistent with the IC/CMB emission mechanism in the on-jet axis regions. Therefore, the fact that (i) $R \pm 1\hat{\sigma} > 0$ for a majority of the sources in the broad band, and (ii) R tends to increase with redshift suggests that (i) the dominant X-ray emission mechanism in the radio lobes is IC/CMB in origin, and that (ii) the non-thermal emission due to IC/CMB from the radio lobes in general tends to dominate the thermal bremsstrahlung emission from the hot gas in the ICM environment of radio galaxies.

There have been various studies suggesting that the X-ray emission mechanism in jets is likely due to the IC upscattering of CMB photons. Tavecchio et al. (2000) and Celotti et al. (2001) used *Chandra* observations of the 100 kpc jet of PKS 0637-752 to propose the IC/CMB mechanism for the jet X-ray emission. Harris & Krawczynski (2002) presented a formulation of anisotropic IC emission from relativistically moving jets, suggesting that the jets have high bulk relativistic velocities on kpc scales, and that higher redshift sources require lower IC beaming compared to lower redshift sources due to the higher CMB energy density. Crosston et al. (2005) used archival *Chandra* and *XMM-Newton* data for a sample of 40 FR II radio galaxies and quasars between $0.05 < z < 2$, and found that the X-ray emission from the radio lobes can be attributed to the IC/CMB mechanism. Kharb et al. (2012b) used deep *Chandra* and *HST* observations of two quasars, PKS B0106+013 and 1641+399 (3C 345), and found that the X-rays from the jets are produced from IC mechanism from relativistically boosted CMB seed photons. Ineson et al. (2017) measured the X-ray lobe IC emission for a sample of 37 FR II galaxies between $0.1 < z < 0.5$ to investigate the internal radio lobe conditions and lobe dynamics. Mingo et al. (2017) studied the X-ray emission associated with the extended structures (jets, lobes, and environments) of 26 sources from the 2 Jy sample of radio galaxies[9] between $0.05 < z < 0.2$, although the FR II lobe analysis in Mingo et al. (2017) was part of the wider FR II lobe study of Ineson et al. (2017).

More recently, Jimenez-Gallardo et al. (2021) studied the extended emission in the $0.5 - 3.0$ keV band with *Chandra* data around 35 FR II radio galaxies between $0.05 < z < 0.9$ selected from the 3CR catalog. About half of their sample overlaps with ours. They found that the non-thermal IC/CMB process dominates in $\sim 70\%$ of the sources in their sample, while the thermal emission from the ICM dominates in $\sim 15\%$ of them. As expected, the results in our study are in general agreement with those of Jimenez-Gallardo et al. (2021).

Thus, our results are consistent with previous work which suggests that the X-ray emission from radio lobes is due to IC scattering of the CMB.

7. SOURCES WITH X-RAY EMISSION ASSOCIATED WITH RADIO HOTSPOTS

During this study, we found some sources with X-ray emission spatially correlated with the radio hotspots. Since in our selection criteria we did not include sources with X-ray emission associated with the radio hotspots, the sources listed below were excluded from the sample.

[9] https://2jy.extragalactic.info/2Jy_home_page.html

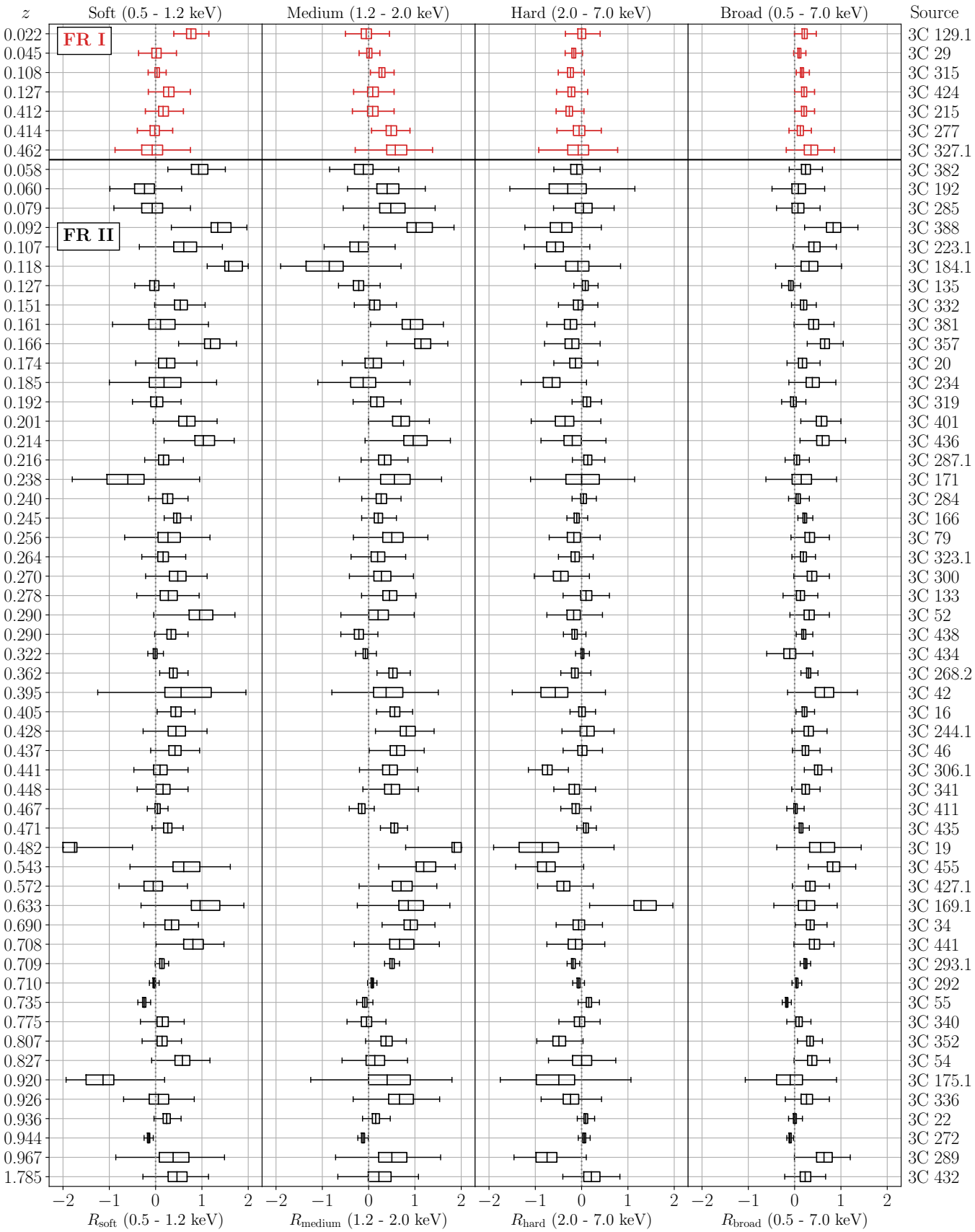


Figure 5. The box plots of R values for the 60 3CR extragalactic radio sources in our sample. See Figure 4 for the box plot definitions.

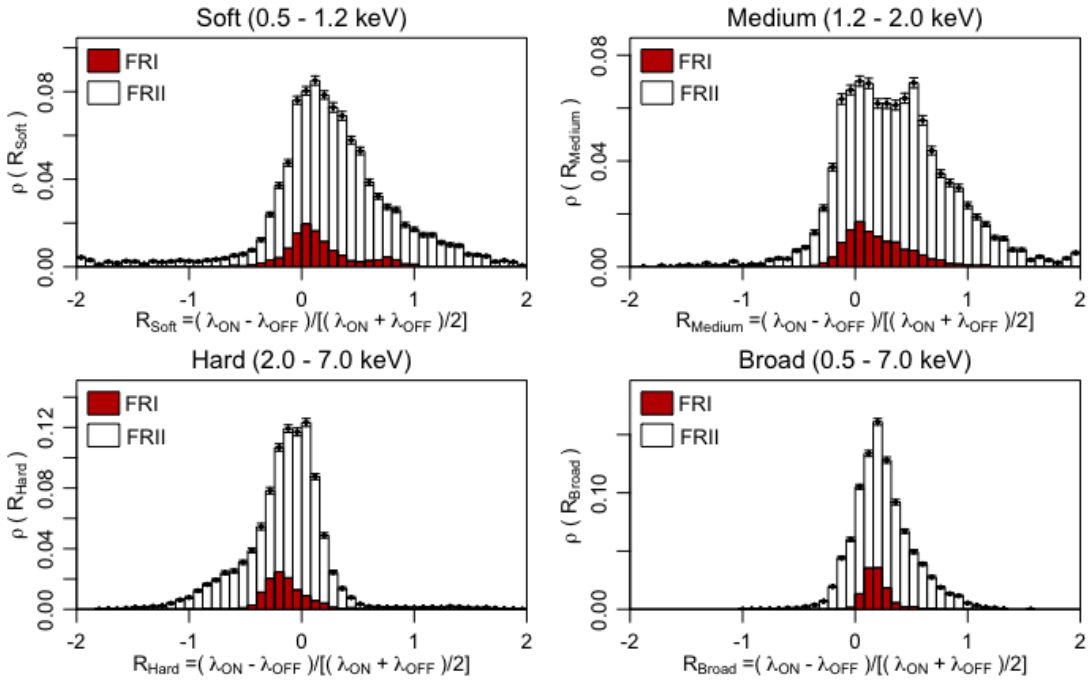


Figure 6. FR I and FR II stacked and normalized histograms of binned R distributions for 7 FR I and 53 FR II sources , where $\rho(R)$ is the probability density. The histograms are generated by taking a random sample from each of the R distribution functions, in a given band, and binning the results in an iterative fashion, until the error in frequency is minimized. The tiny error-bars on top of each histogram-bar indicate the bin uncertainties after 250 iterations. Examples of individual R distribution functions are given in Figures 3 and 4.

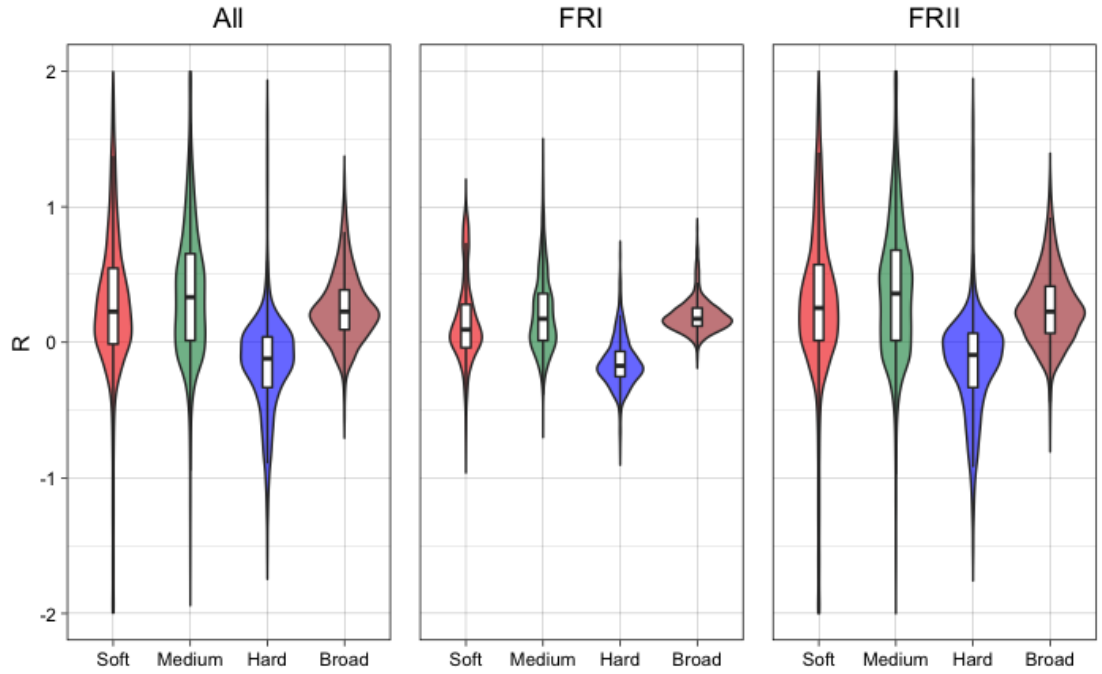


Figure 7. Summary violin plots of Figure 6, where the embedded box-plot median-R values with their 1st (Q1) and 3rd (Q3) quartile ranges are given in Table 1. The lower and upper whiskers are given by the usual $Q1 - (1.5 \times IQR)$ and $Q3 + (1.5 \times IQR)$, respectively, where IQR is the Interquartile Range (i.e., $Q3 - Q1$). For both FR I and FR II sources, in general, it can be seen that the soft, medium, and broad bands favor $R > 0$, whereas the hard band favors $R < 0$.

3C 41: Southeast hotspot.
3C 153: Northeast hotspot.
3C 263.1: Northeast and southwest hotspots.
3C 337: Southeast hotspot.

We also confirm the presence of X-ray emission associated with the radio hotspots of the following sources previously reported in Massaro et al. (2015a).

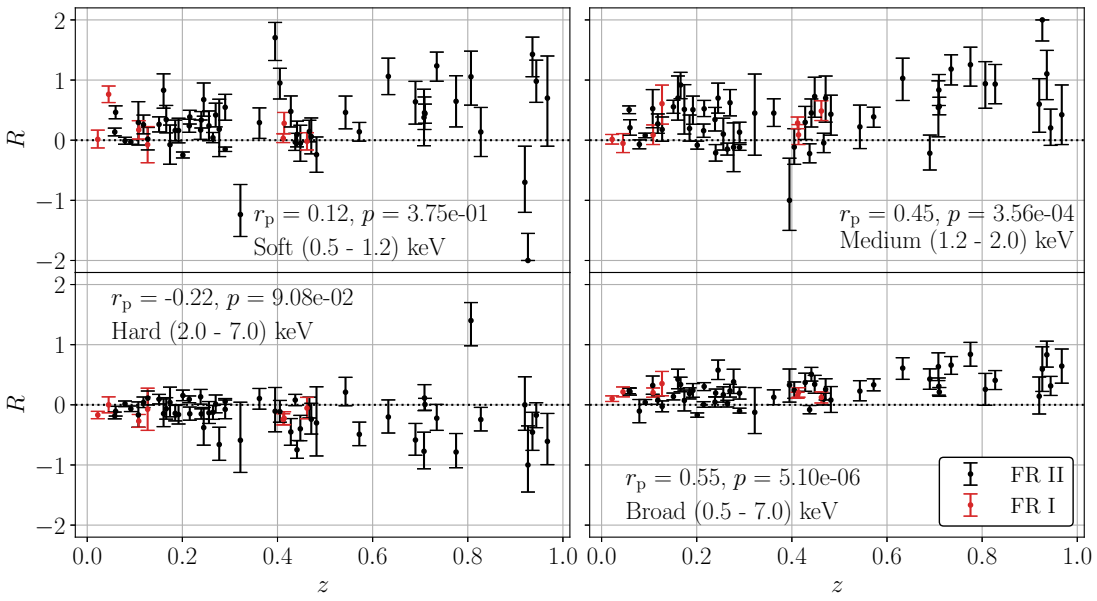


Figure 8. R as a function of redshift.

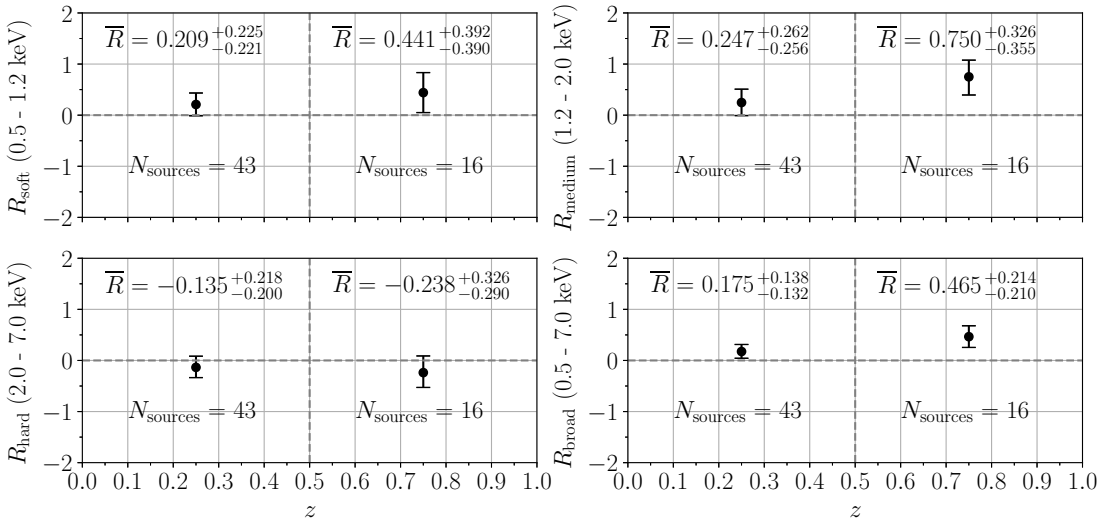


Figure 9. $\overline{R}$ as a function of redshift in two redshift bins: (i) $0 < z < 0.5$ and (ii) $0.5 < z < 1.0$. The source 3C 432, which has a redshift of 1.785, was excluded in these calculations in order to simplify the redshift bins, since 3C 432 is the only source in our sample with redshift greater than 1. Here, $\overline{R}$ is the average of the R values for all sources in that particular redshift bin, and the errorbars on $\overline{R}$ are the $\pm 1\hat{\sigma}$ errorbars of all the sources in that particular redshift bin added in quadrature. The broad band has the highest signal-to-noise ratio and hence the smallest errorbars. $\overline{R}$ tends to increase with z in the broad band, suggesting that the on-axis jet emission is due to the inverse Compton scattering of CMB photons by hot electrons, a process for which the observed flux is roughly redshift independent due to the increasing CMB energy density with z.

3C 299: Northeast and southwest hotspots.
3C 325: Northwest and southeast hotspots.
3C 349: Southeast hotspot.

These sources were also excluded from our sample. Figures 11-17 show the broadband X-ray images with overlaid radio contours of the sources mentioned above.

8. SUMMARY

This paper studied the extended faint X-ray emission associated with the radio lobes and the hot gas in the ICM environment for a sample of 60 radio galaxies (7 FR I and 53 FR II) selected from the 298 extragalactic radio sources identified in the 3CR catalog. We looked for any asymmetry in the extended faint X-ray emission between regions that contain the radio lobes and regions in the hot environment that do not contain the radio lobes.

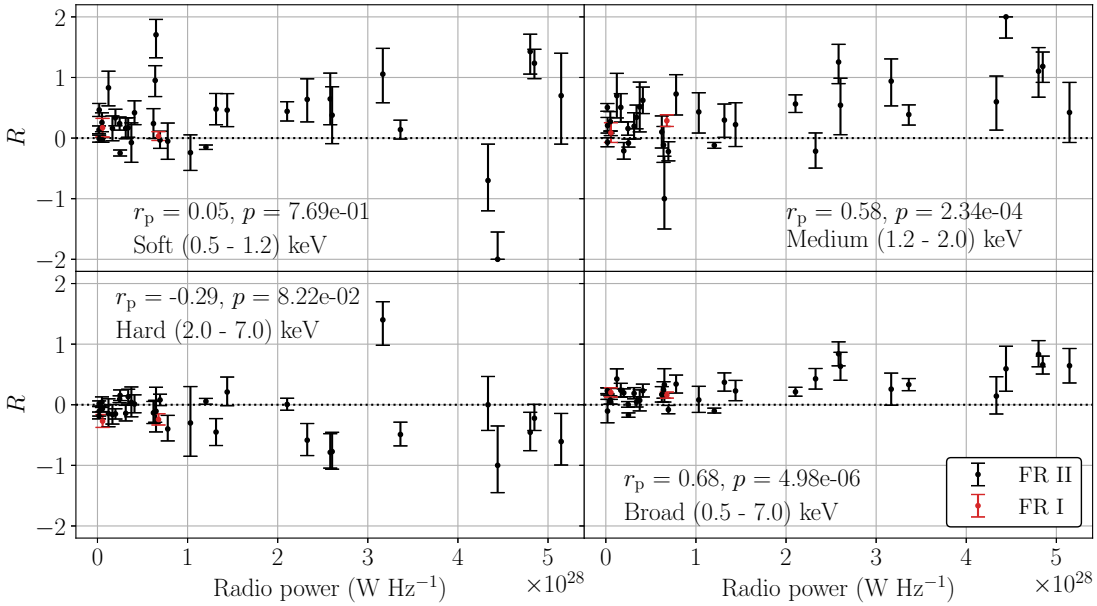


Figure 10. R as a function of radio power.

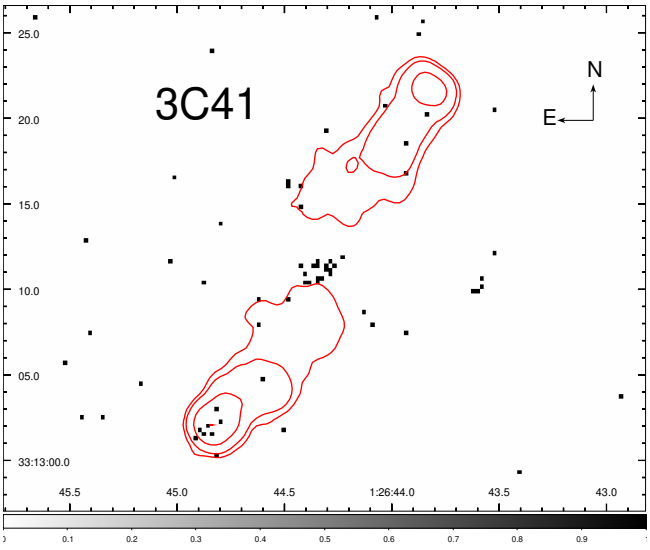


Figure 11. 3C 41 broad band X-ray image with radio contours in red. X-ray and radio emission spatial correlation in south-east hotspot.

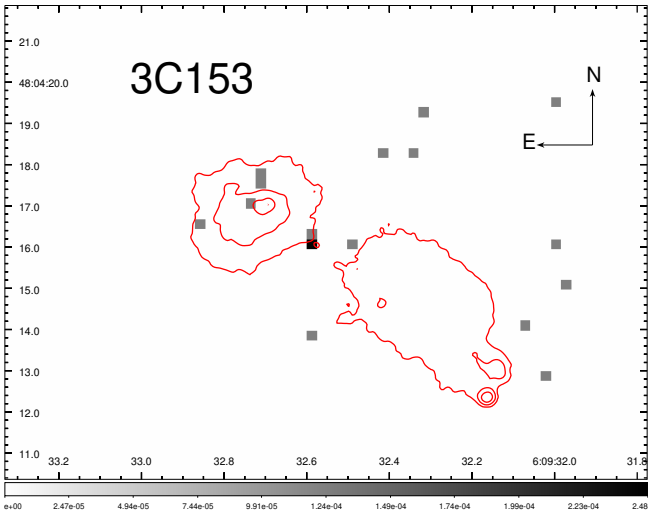


Figure 12. 3C 153 broad band X-ray image with radio contours in red. X-ray and radio emission spatial correlation in north-east radio hotspot.

To do so, we constructed a circular science aperture for each source with four quadrants of equal area, where two quadrants contain the radio lobes (on-jet axis) and the two other quadrants do not contain the radio lobes and are in the environment regions (off-jet axis). We used shallow ($\sim$ 10 ks) archival X-ray observations from *Chandra* for our sample in four energy bands: soft ($0.5-1.2$ keV), medium ($1.2-2.0$ keV), hard ($2.0-7.0$ keV), and broad ($0.5-7.0$ keV). The radio images were taken with the VLA.

We used Bayesian techniques on the Poission X-ray counts in the on and off-jet axis regions to determine whether the on-jet axis or the off-jet axis emission dominates for each source and each band. To do so, we used the parameter R, defined as $R = (S_{\rm ON} - S_{\rm OFF}) \,/\, [(S_{\rm ON} + S_{\rm OFF}) \,/\, 2]$, such that $R > 0$ corresponds to higher on-jet axis emission (from the radio lobes) and $R < 0$ corresponds to higher off-jet axis emission (from the hot gas in the environment). Since the broad band had the most detected photons and therefore the highest signal-to-noise ratio, we focus our physical interpretation using the broad band results.

We found that the non-thermal X-ray emission from the radio lobes dominates the thermal X-ray emission from the hot gas in the ICM for a majority ($\sim$ 77%) of

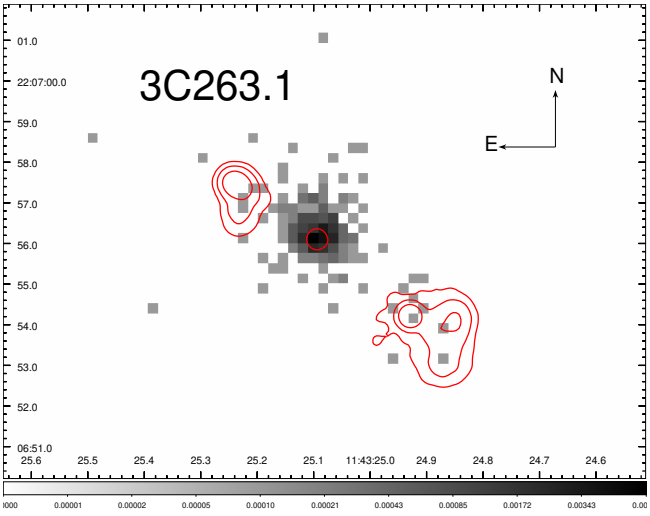


Figure 13. 3C 263.1 broad band X-ray image with radio contours in red. X-ray and radio emission spatial correlation in north-east and south-west radio hotspots.

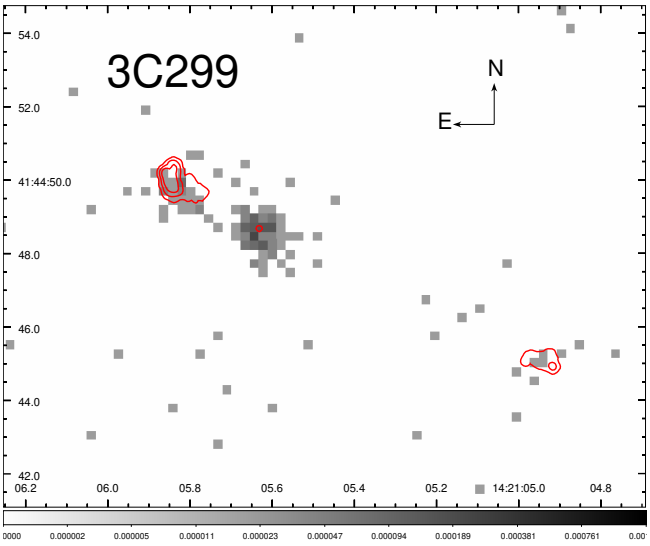


Figure 14. 3C 299 broad band X-ray image with radio contours in red. X-ray and radio emission spatial correlation in north-east and south-west radio hotspots.

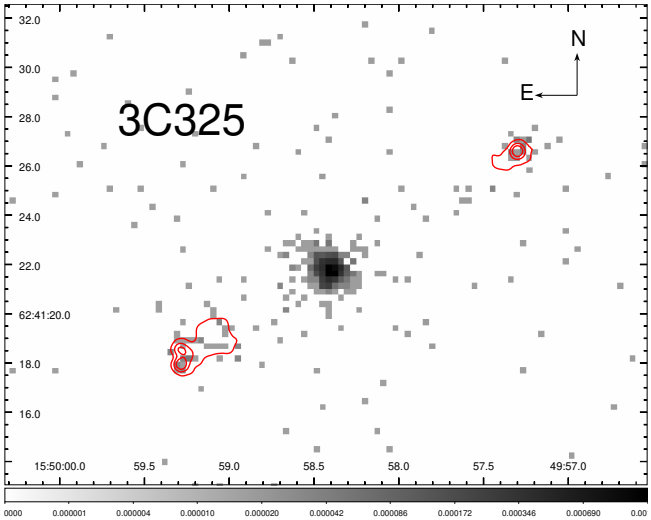


Figure 15. 3C 325 broad band X-ray image with radio contours in red. X-ray and radio emission spatial correlation in north-west and south-east radio hotspots.

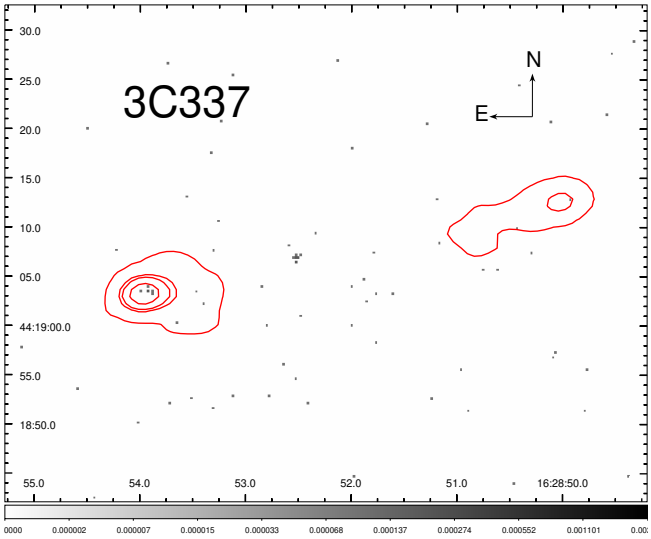


Figure 16. 3C 337 broad band X-ray image with radio contours in red. X-ray and radio emission spatial correlation in south-east radio hotspot.

sources in the combined FR I and FR II sample. The thermal X-ray emission from the ICM dominates the non-thermal X-ray lobe emission for only $\sim 5\%$ of the sources in the combined sample.

We also found that R in the broad band has a marginal increase with increasing redshift. The observed flux due to the off-jet axis thermal bremsstrahlung emission from the hot gas in the environment can be expected to decrease with increasing redshift. On the other hand, the observed flux due to the on-jet axis inverse Compton scattering of CMB seed photons by relativistic electrons in the radio lobes is roughly independent of redshift, due to the increasing CMB energy density at increasing redshift. The fact that R tends to increase with increasing redshift suggests that dominant X-ray emission mechanism in the radio lobes is IC/CMB in origin. Therefore, our results suggest that the non-thermal X-ray emission due to the IC/CMB process from the radio lobes in general tends to dominate the thermal X-ray emission from the hot gas in the ICM environment of radio galaxies. Our results are consistent with previous work.

9. ACKNOWLEDGMENTS

We thank the referee for detailed comments which helped to improve the paper. We thank Dr. Francesco Massaro for his comments and for providing radio im-

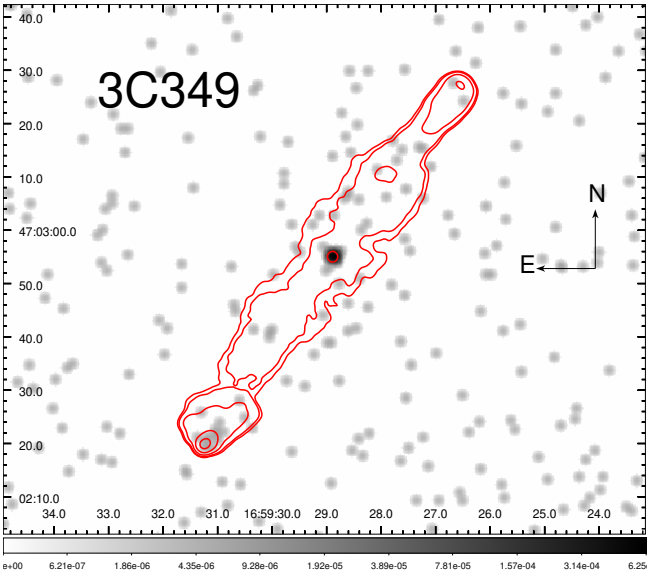


Figure 17. 3C 349 broad band X-ray image smoothed with a Gaussian. Radio contours in red. X-ray and radio emission spatial correlation in south-east radio hotspot.

ages for some sources, and Dr. Adrian Vantyghem for his feedback regarding interpretation of the Bayesian analysis results. This work used archival data from *Chandra* and software provided by the *Chandra* X-ray Center (CXC) in the application package CIAO. `SAOImage DS9` was used for the analysis of the X-ray and radio data. `SAOImage DS9` was developed by the Smithsonian Astrophysical Observatory (Joye & Mandel 2003). Many radio images were downloaded from NVAS. The National Radio Astronomy Observatory is operated by Associated Universities, Inc., under contract with the National Science Foundation. The research for this paper involved the use of NASA's Astrophysical Data System and the NASA/IPAC Extragalactic Database (NED) provided by the Jet Propulsion Laboratory, California Institute of Technology, under contract with the National Aeronautics and Space Administration. The research of Drs. S. Baum, M. Boyce, and C. O'Dea was supported by the Natural Sciences and Engineering Research Council (NSERC) of Canada.

APPENDIX

A. BAYESIAN ANALYSIS

Application of Bayesian analysis in astronomy is rapidly expanding in its areas of influence, and, as such, is useful to have in one's toolkit. However, it can have a steep learning curve. In the area of X-ray astronomy, dealing with low statistics, authors, such as, van Dyk et al. (2001) and Park et al. (2006) have paved the way, providing theory and application examples. In this appendix, their work is extended by providing a case study of the prior distribution function, Equation (4), for the jet-axes ratio, R, Equation (1).

In the derivation of Equation (4), the source, S_x, and background, B_x, counts are modeled in terms of their expected source, λ_x, and background, ξ_x, counts, respectively, as

$$\left.\begin{array}{rcl} S_x & \overset{d}{\sim} & \mathrm{Poisson}(e_C\,(\lambda_x+\xi_x)) \\ B_x & \overset{d}{\sim} & \mathrm{Poisson}(r\,e_C\,\xi_x) \end{array}\right\}, \tag{A1}$$

where $x = \mathrm{ON}, \mathrm{OFF}$, $r = 2$ (see discussion in Section 4.4) is a scale factor that accounts for the differences in source and background measurement areas and sensitivities, and $e_C = 1$ (see discussion in Section 2.1 of Park et al. (2006)) is an instrumental parameter that accounts for the variations in the soft (e_S), medium (e_M), hard (e_H), and broad (e_B) band (i.e., $C = S, M, H, B$) effective areas, exposure times, etc. This approach is justified, as the sum of two independent Poisson random variables (*i.e.*, λ_x and ξ_x) is a Poisson random variable (*i.e.*, $\lambda_x + \xi_x$) (Hoff 2010), and so we may express Equation (1) as

$$R = \frac{\lambda_{\mathrm{ON}} - \lambda_{\mathrm{OFF}}}{(\lambda_{\mathrm{ON}} + \lambda_{\mathrm{OFF}})/2}\,. \tag{A2}$$

The joint posterior distribution of λ_x and ξ_x, given prior knowledge S_x and B_x, can be expressed using the Bayes' Theorem (Park et al. 2006) as

$$P(\lambda_x,\,\xi_x|S_x,B_x) = \frac{P(\lambda_x,\,\xi_x)\,P(S_x,B_x|\lambda_x,\,\xi_x)}{\int\int P(\lambda'_x,\,\xi'_x)\,P(S_x,B_x|\lambda'_x,\,\xi'_x)\,d\lambda'_x\,d\xi'_x}\,. \tag{A3}$$

where $P(S_x,B_x|\lambda_x,\,\xi_x) = P(S_x|\lambda_x,\,\xi_x)\,P(B_x|\xi_x)$ (see Equation (A1)) is the likelihood of observing S_x and B_x given λ_x and ξ_x, and $P(\lambda_x,\,\xi_x)$ is our prior probability distribution function. In order for the posterior distribution to have the same parametric form as the likelihood functions, Equation (A1) $\overset{d}{\sim}$ Poissonian, we model λ_x and ξ_x using conjugate gamma-prior distributions as

$$\left.\begin{array}{rcl} \lambda_x & \overset{d}{\sim} & \gamma(\psi_{S_{x_1}},\psi_{S_{x_2}}) \\ \xi_x & \overset{d}{\sim} & \gamma(\psi_{S_{x_3}},\psi_{S_{x_4}}) \end{array}\right\}, \tag{A4}$$

with the hyperparameters

$$\left.\begin{array}{l} \psi_{S_{x_1}} = S_x + 1 \\ \psi_{S_{x_2}} = 1 \\ \psi_{S_{x_3}} = B_x + 1 \\ \psi_{S_{x_4}} = 1 \end{array}\right\}, \tag{A5}$$

where λ_x and ξ_x are assumed to be a priori independent, *i.e.*, $P(\lambda_x,\,\xi_x) = P(\lambda_x)\,P(\xi_x)$, van Dyk et al. (2001).[10] We note at this point, that the analysis being done here, is similar to that of Park et al. (2006), except they are computing harness ratios

$$\mathcal{HR} = \frac{\lambda_{\mathrm{H}} - \lambda_{\mathrm{S}}}{\lambda_{\mathrm{H}} + \lambda_{\mathrm{S}}}\,, \tag{A6}$$

[10] Assuming an informative model: *i.e.*, we have measured background counts, B_x.

where $\lambda_{\rm H}$ and $\lambda_{\rm S}$ are the expected hard and soft band counts, respectively, which is analogous in form to Equation (A2), with the equivalence $\lambda_{\rm ON} \Leftrightarrow \lambda_{\rm H}$ and $\lambda_{\rm OFF} \Leftrightarrow \lambda_{\rm S}$. So comparing Equation (A3) with Equation (A6) of Park et al. (2006), we obtain the analytical expression

$$P(\lambda_x|S_x\,B_x) = \frac{\displaystyle\sum_{\ell=0}^{S_x} \frac{1}{\Gamma(\ell+1)\Gamma(S_x-\ell+1)} \frac{\Gamma(S_x-\ell+B_x+\psi_{S_{x_3}})}{(e_C+r\,e_C+\psi_{S_{x_4}})^{S_x-\ell+B_x+\psi_{S_{x_3}}}} \lambda_x^{\ell+\psi_{S_{x_1}}-1}\, e^{-(e_C+\psi_{S_{x_2}})\lambda_x}}{\displaystyle\sum_{k=0}^{S_x} \frac{1}{\Gamma(k+1)\Gamma(S_x-k+1)} \frac{\Gamma(S_x-k+B_x+\psi_{S_{x_3}})}{(e_C+r\,e_C+\psi_{S_{x_4}})^{S_x-k+B_x+\psi_{S_{x_3}}}} \frac{\Gamma(k+\psi_{S_{x_1}})}{(e_C+\psi_{S_{x_2}})^{k+\psi_{S_{x_1}}}}}\,, \tag{A7}$$

where the nuisance parameter, ξ_x, has been integrated out. Our joint distribution for our expected ON/OFF counts is given by

$$P(\lambda_{\rm ON},\lambda_{\rm OFF}|S_{\rm ON},S_{\rm OFF},B_{\rm ON},B_{\rm OFF}) = P(\lambda_{\rm ON}|S_{\rm ON},B_{\rm ON})\,P(\lambda_{\rm OFF}|S_{\rm OFF},B_{\rm OFF})\,, \tag{A8}$$

assuming $\lambda_{\rm ON}$ and $\lambda_{\rm OFF}$ are a priori independent. Figure (18) shows example plots for sources 3C 401 and 3C 22 for the broad and soft bands, respectively.

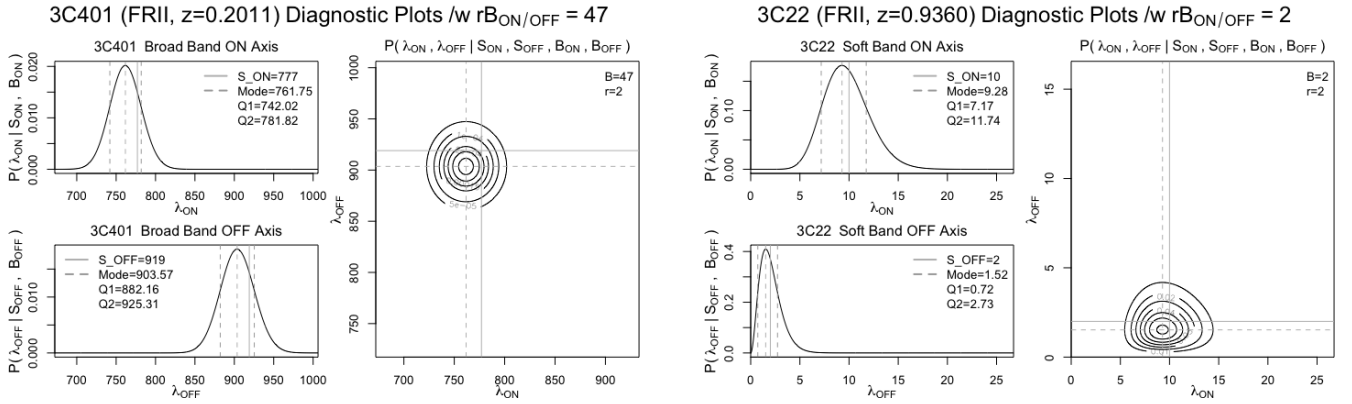


Figure 18. Example plots of Equation (A8) for sources 3C 401 (left panel) and 3C 22 (right panel) for the broad and soft bands, respectively, with input values from Table 5. The probability distributions $P(\lambda_{\rm ON}|S_{\rm ON},B_{\rm ON})$, $P(\lambda_{\rm OFF}|S_{\rm OFF},B_{\rm OFF})$, and $P(\lambda_{\rm ON},\lambda_{\rm OFF}|S_{\rm ON},S_{\rm OFF},B_{\rm ON},B_{\rm OFF})$ are plotted in the top-left, bottom-left, and right sub-plots of the panels, respectively. The grey solid-lines show input $S_{\rm ON/OFF}$ values, and the dashed-lines show the expected $\lambda_{\rm ON/OFF}$ mode-values with 68.27% HPD ($\sim 1\sigma$) boundaries.

Equation (A8) simplifies to

$$P(\lambda_{\rm ON},\lambda_{\rm OFF}|S_{\rm ON},S_{\rm OFF},B) = P(\lambda_{\rm ON}|S_{\rm ON},B)\,P(\lambda_{\rm OFF}|S_{\rm OFF},B)\,, \tag{A9}$$

as $B_{\rm ON} = B_{\rm OFF} = B/r$, Equation (3), and so

$$P(\lambda_{\rm ON},\lambda_{\rm OFF}|S_{\rm ON},S_{\rm OFF},B) = \sum_{i=0}^{S_{\rm ON}}\sum_{j=0}^{S_{\rm OFF}} N(i,S_{\rm ON},B)N(j,S_{\rm OFF},B)\lambda_{\rm ON}^{\alpha_{\rm ON}(i)}\lambda_{\rm OFF}^{\alpha_{\rm OFF}(j)}e^{-\beta(\lambda_{\rm ON}+\lambda_{\rm OFF})} \tag{A10}$$

where

$$N(\ell,S_x,B) = \frac{\dfrac{1}{\Gamma(\ell+1)\Gamma(S_x-\ell+1)} \dfrac{\Gamma(S_x-\ell+B+\psi_{S_{x_3}})}{(e_C+r\,e_C+\psi_{S_{x_4}})^{S_x-\ell+B+\psi_{S_{x_3}}}}}{\displaystyle\sum_{k=0}^{S_x} \frac{1}{\Gamma(k+1)\Gamma(S_x-k+1)} \frac{\Gamma(S_x-k+B+\psi_{S_{x_3}})}{(e_C+r\,e_C+\psi_{S_{x_4}})^{S_x-k+B+\psi_{S_{x_3}}}} \frac{\Gamma(k+\psi_{S_{x_1}})}{(e_C+\psi_{S_{x_2}})^{k+\psi_{S_{x_1}}}}}\,, \tag{A11}$$

$$\alpha_x(\ell) = \ell + \psi_{S_{x_1}} - 1\,, \tag{A12}$$

and

$$\beta = e_C + \psi_{S_2}\,, \tag{A13}$$

with $\psi_{S_2} \equiv \psi_{S_{x_2}} = 1$, and $\ell = i, j$. Now, we need to transform Equation (A10) to our ON/OFF jet-axis ratio R, Equation (A2). Again, leveraging the work of Park et al. (2006), by using their transform

$$\begin{aligned} P(\lambda_{\rm S}, \lambda_{\rm H}|S, H, B_{\rm S}, B_{\rm H})\, d\lambda_{\rm S}\, d\lambda_{\rm H} &= P(\lambda_{\rm S}(\mathcal{HR}, \omega'), \lambda_{\rm H}(\mathcal{HR}, \omega')|S, H, B_{\rm S}, B_{\rm H}) \left|\frac{\partial(\lambda_{\rm S}, \lambda_{\rm H})}{\partial(\mathcal{HR}, \omega')}\right| d(\mathcal{HR}) d\omega' \\ &= P\left(\frac{(1-\mathcal{HR})\omega'}{2}, \frac{(1+\mathcal{HR})\omega'}{2}\middle| S, H, B_{\rm S}, B_{\rm H}\right)\frac{\omega'}{2} d(\mathcal{HR}) d\omega' \end{aligned} \tag{A14}$$

where

$$\omega' = \lambda_{\rm H} + \lambda_{\rm S}\,, \tag{A15}$$

we then obtain

$$P(\lambda_{\rm ON}, \lambda_{\rm OFF}|S_{\rm ON}, S_{\rm OFF}, B)\, d\lambda_{\rm ON}\, d\lambda_{\rm OFF} = P\left(\left(1+\frac{R}{2}\right)\omega, \left(1-\frac{R}{2}\right)\omega\,\middle|\, S_{\rm ON}, S_{\rm OFF}, B\right)\omega\, dR\, d\omega\,, \tag{A16}$$

where

$$\omega = \frac{\lambda_{\rm ON} + \lambda_{\rm OFF}}{2}\,. \tag{A17}$$

So integrating out ω, we have

$$\begin{aligned} P(R|S_{\rm ON}, S_{\rm OFF}, B) &= \sum_{i=0}^{S_{\rm ON}}\sum_{j=0}^{S_{\rm OFF}} \Lambda_{ij}(S_{\rm ON}, S_{\rm OFF}, B) \int_0^\infty \left[\left(1+\frac{R}{2}\right)\omega\right]^{\alpha_{\rm ON}(i)} \left[\left(1-\frac{R}{2}\right)\omega\right]^{\alpha_{\rm OFF}(j)} \\ &\quad \times e^{-\beta\left[\left(1+\frac{R}{2}\right)\omega + \left(1-\frac{R}{2}\right)\omega\right]}\, \omega\, d\omega \\ &= \sum_{i=0}^{S_{\rm ON}}\sum_{j=0}^{S_{\rm OFF}} \Lambda_{ij}(S_{\rm ON}, S_{\rm OFF}, B) \left(1+\frac{R}{2}\right)^{\alpha_{\rm ON}(i)} \left(1-\frac{R}{2}\right)^{\alpha_{\rm OFF}(j)} \int_0^\infty \omega^{\alpha_{\rm ON}(i)+\alpha_{\rm OFF}(j)+1} e^{-2\beta\omega} d\omega \\ &= \sum_{i=0}^{S_{\rm ON}}\sum_{j=0}^{S_{\rm OFF}} \kappa_{ij}(S_{\rm ON}, S_{\rm OFF}, B, R) \int_0^\infty \omega^{\eta_{ij}-1} e^{-2\beta\omega} d\omega\,, \end{aligned} \tag{A18}$$

where

$$\Lambda_{ij}(S_{\rm ON}, S_{\rm OFF}, B) = N(i, S_{\rm ON}, B) N(j, S_{\rm OFF})\,, \tag{A19}$$

$$\kappa_{ij}(S_{\rm ON}, S_{\rm OFF}, B, R) = \Lambda_{ij}(S_{\rm ON}, S_{\rm OFF}, B) \left(1+\frac{R}{2}\right)^{\alpha_{\rm ON}(i)} \left(1-\frac{R}{2}\right)^{\alpha_{\rm OFF}(j)}\,, \tag{A20}$$

and

$$\eta_{ij} = \alpha_{\rm ON}(i) + \alpha_{\rm OFF}(j) + 2\,, \tag{A21}$$

leaving us with $\int_0^\infty \omega^{\eta_{ij}-1} e^{-2\beta\omega} d\omega$ to evaluate. So,

$$\begin{aligned} \int_0^\infty \omega^{\eta_{ij}-1} e^{-2\beta\omega} d\omega &= \int_0^\infty \frac{(2\beta\omega)^{\eta_{ij}-1}}{(2\beta)^{\eta_{ij}-1}} e^{-(2\beta\omega)} \frac{d(2\beta\omega)}{2\beta} = \frac{1}{(2\beta)^{\eta_{ij}}} \int_0^\infty x^{\eta_{ij}-1} e^{-x} dx = \frac{1}{(2\beta)^{\eta_{ij}}}\Gamma(\eta_{ij}) \\ &= \frac{\Gamma(\alpha_{\rm ON}(i) + \alpha_{\rm OFF}(j) + 2)}{(2\beta)^{\alpha_{\rm ON}(i)+\alpha_{\rm OFF}(j)+2}} = \frac{\Gamma(i + j + \psi_{S_{\rm ON_1}} + \psi_{S_{\rm OFF_1}})}{[2(e_C + \psi_{S_2})]^{i+j+\psi_{S_{\rm ON_1}}+\psi_{S_{\rm OFF_1}}}}\,. \end{aligned} \tag{A22}$$

Therefore,

$$P(R|S_{\rm ON},S_{\rm OFF},B)=\sum_{i=0}^{S_{\rm ON}}\sum_{j=0}^{S_{\rm OFF}}\kappa_{ij}(S_{\rm ON},S_{\rm OFF},B,R)\frac{\Gamma(i+j+\psi_{S_{{\rm ON}_1}}+\psi_{S_{{\rm OFF}_1}})}{[2(e_C+\psi_{S_2})]^{i+j+\psi_{S_{{\rm ON}_1}}+\psi_{S_{{\rm OFF}_1}}}}\,, \tag{A23}$$

where

$$\kappa_{ij}(S_{\rm ON},S_{\rm OFF},B,R)=N(i,S_{\rm ON},B)N(j,S_{\rm OFF},B)\left(1+\frac{R}{2}\right)^{i+\psi_{S_{{\rm ON}_1}}-1}\left(1-\frac{R}{2}\right)^{j+\psi_{S_{{\rm OFF}_1}}-1}\,, \tag{A24}$$

and

$$N(\ell,S_x,B)=\frac{\dfrac{\Gamma(S_x-\ell+B+\psi_{S_{x_3}})}{\Gamma(\ell+1)\Gamma(S_x-\ell+1)(e_C+r\,e_C+\psi_{S_{x_4}})^{S_x-\ell+B+\psi_{S_{x_3}}}}}{\displaystyle\sum_{k=0}^{S_x}\frac{\Gamma(S_x-k+B+\psi_{S_{x_3}})\Gamma(k+\psi_{S_{x_1}})}{\Gamma(k+1)\Gamma(S_x-k+1)(e_C+r\,e_C+\psi_{S_{x_4}})^{S_x-k+B+\psi_{S_{x_3}}}(e_C+\psi_{S_{x_2}})^{k+\psi_{S_{x_1}}}}}\,. \tag{A25}$$

Finally, substituting $r=2$, $e_C=1$, and Equations (A5) into above, we obtain Equation (4). Figures (3) and (4) show examples of the posterior distributions for $R_{\rm broad}^{\rm 3C401}$ and $R_{\rm soft}^{\rm 3C22}$, respectively, which can be contrasted with Figure (18).

Coding up Equation (4) is pretty straightforward, except one needs to pay careful attention to the Γ functions and powers, so as to avoid rounding errors. It is recommended one use an arbitrary precision library, such as, `mpmath`.[11] Herein, we also use the Gaussian approximation, Equation (5), for counts $S_{\rm ON}+S_{\rm OFF}>2000$. Figure 5 and Table 3 summarize the results.

B. R VALUES

Table 3 shows the R values for the sources in our sample for the different *Chandra* energy bands.

Table 3. R values (*i.e.*, modes) for soft, medium, hard, and broad bands, computed using Equations (4) and (5)† with input counts from Table 5. The error limits are given by the 68.27% HPD bounds for Equation (4) and by the $\pm1\sigma$ bounds for Equation (5).

Source	z	FR type	$R_{\rm soft}$	$R_{\rm medium}$	$R_{\rm hard}$	$R_{\rm broad}$
3C 16	0.4050	FR II	$+0.95^{+0.24}_{-0.27}$	$-0.11^{+0.31}_{-0.29}$	$-0.11^{+0.19}_{-0.18}$	$+0.24^{+0.14}_{-0.14}$
3C 19	0.4820	FR II	$-0.24^{+0.29}_{-0.29}$	$+0.43^{+0.32}_{-0.35}$	$-0.30^{+0.60}_{-0.55}$	$+0.08^{+0.22}_{-0.21}$
3C 20	0.1740	FR II	$-0.07^{+0.33}_{-0.33}$	$+0.51^{+0.41}_{-0.41}$	$+0.04^{+0.25}_{-0.24}$	$+0.07^{+0.17}_{-0.17}$
3C 22	0.9360	FR II	$+1.43^{+0.29}_{-0.37}$	$+1.10^{+0.39}_{-0.43}$	$-0.46^{+0.33}_{-0.30}$	$+0.83^{+0.23}_{-0.21}$
3C 29	0.0450	FR I	$+0.76^{+0.14}_{-0.14}$	$-0.05^{+0.16}_{-0.15}$	$+0.00^{+0.13}_{-0.13}$	$+0.22^{+0.08}_{-0.08}$
3C 34	0.6900	FR II	$+0.64^{+0.34}_{-0.37}$	$-0.22^{+0.30}_{-0.28}$	$-0.58^{+0.27}_{-0.25}$	$+0.43^{+0.17}_{-0.17}$
3C 42	0.3950	FR II	$+1.70^{+0.25}_{-0.38}$	$-1.00^{+0.70}_{-0.50}$	$-0.11^{+0.39}_{-0.34}$	$+0.33^{+0.27}_{-0.28}$
3C 46	0.4373	FR II	$-0.03^{+0.15}_{-0.14}$	$-0.22^{+0.16}_{-0.15}$	$+0.08^{+0.09}_{-0.09}$	$-0.08^{+0.07}_{-0.07}$
3C 52	0.2900	FR II	$+0.55^{+0.21}_{-0.21}$	$+0.13^{+0.17}_{-0.18}$	$-0.08^{+0.16}_{-0.16}$	$+0.19^{+0.10}_{-0.10}$
3C 54	0.8274	FR II	$+0.14^{+0.41}_{-0.41}$	$+0.93^{+0.33}_{-0.33}$	$-0.24^{+0.20}_{-0.19}$	$+0.41^{+0.16}_{-0.15}$
3C 55	0.7348	FR II	$+1.24^{+0.23}_{-0.25}$	$+1.18^{+0.24}_{-0.26}$	$-0.22^{+0.23}_{-0.20}$	$+0.66^{+0.14}_{-0.15}$
3C 79	0.2559	FR II	$+0.24^{+0.25}_{-0.25}$	$+0.10^{+0.26}_{-0.26}$	$-0.13^{+0.19}_{-0.18}$	$+0.17^{+0.13}_{-0.12}$
3C 129.1	0.0222	FR I	$+0.01^{+0.15}_{-0.14}$	$+0.01^{+0.08}_{-0.08}$	$-0.17^{+0.06}_{-0.06}$	$+0.10^{+0.05}_{-0.05}$
3C 133	0.2775	FR II	$+0.18^{+0.50}_{-0.45}$	$-0.12^{+0.41}_{-0.41}$	$-0.66^{+0.29}_{-0.26}$	$+0.38^{+0.21}_{-0.19}$

[11] `https://mpmath.org`

Table 3. (*Continued...*)

Source	z	FR type	$R_{\rm soft}$	$R_{\rm medium}$	$R_{\rm hard}$	$R_{\rm broad}$
3C 135	0.1273	FR II	$+0.02^{+0.19}_{-0.18}$	$+0.18^{+0.21}_{-0.20}$	$+0.11^{+0.12}_{-0.11}$	$-0.03^{+0.09}_{-0.09}$
3C 166	0.2449	FR II	$+0.68^{+0.28}_{-0.28}$	$+0.70^{+0.25}_{-0.25}$	$-0.38^{+0.33}_{-0.29}$	$+0.58^{+0.17}_{-0.16}$
3C 169.1	0.6330	FR II	$+1.06^{+0.30}_{-0.30}$	$+1.03^{+0.33}_{-0.37}$	$-0.20^{+0.28}_{-0.27}$	$+0.61^{+0.17}_{-0.19}$
3C 171	0.2384	FR II	$+0.17^{+0.17}_{-0.16}$	$+0.34^{+0.20}_{-0.19}$	$+0.13^{+0.12}_{-0.12}$	$+0.05^{+0.09}_{-0.08}$
3C 175.1	0.9200	FR II	$-0.70^{+0.60}_{-0.50}$	$+0.60^{+0.42}_{-0.47}$	$+0.00^{+0.47}_{-0.42}$	$+0.14^{+0.32}_{-0.30}$
3C 184.1	0.1182	FR II	$+0.26^{+0.16}_{-0.15}$	$+0.27^{+0.17}_{-0.16}$	$+0.04^{+0.09}_{-0.09}$	$+0.08^{+0.07}_{-0.07}$
3C 192	0.0597	FR II	$+0.46^{+0.11}_{-0.11}$	$+0.21^{+0.13}_{-0.12}$	$-0.11^{+0.08}_{-0.08}$	$+0.22^{+0.06}_{-0.06}$
3C 215	0.4121	FR I	$+0.03^{+0.08}_{-0.07}$	$+0.29^{+0.10}_{-0.09}$	$-0.24^{+0.09}_{-0.09}$	$+0.16^{+0.05}_{-0.05}$
3C 223.1	0.1075	FR II	$+0.29^{+0.35}_{-0.37}$	$+0.52^{+0.32}_{-0.32}$	$-0.17^{+0.22}_{-0.20}$	$+0.32^{+0.16}_{-0.15}$
3C 234	0.1849	FR II	$+0.16^{+0.17}_{-0.17}$	$+0.19^{+0.22}_{-0.21}$	$-0.14^{+0.13}_{-0.12}$	$+0.19^{+0.10}_{-0.09}$
3C 244.1	0.4280	FR II	$+0.48^{+0.26}_{-0.26}$	$+0.30^{+0.26}_{-0.28}$	$-0.45^{+0.22}_{-0.22}$	$+0.37^{+0.16}_{-0.15}$
3C 268.2	0.3620	FR II	$+0.29^{+0.24}_{-0.26}$	$+0.45^{+0.24}_{-0.22}$	$+0.10^{+0.17}_{-0.18}$	$+0.13^{+0.12}_{-0.12}$
3C 272	0.9440	FR II	$+0.98^{+0.35}_{-0.35}$	$+0.20^{+0.31}_{-0.29}$	$-0.17^{+0.21}_{-0.21}$	$+0.31^{+0.16}_{-0.16}$
3C 277	0.4140	FR I	$+0.28^{+0.18}_{-0.17}$	$+0.09^{+0.17}_{-0.16}$	$-0.22^{+0.11}_{-0.10}$	$+0.21^{+0.08}_{-0.08}$
3C 284	0.2398	FR II	$+0.34^{+0.14}_{-0.13}$	$-0.21^{+0.14}_{-0.14}$	$-0.15^{+0.08}_{-0.08}$	$+0.20^{+0.07}_{-0.06}$
3C 285	0.0794	FR II	$-0.01^{+0.06}_{-0.06}$	$-0.07^{+0.07}_{-0.07}$	$+0.02^{+0.05}_{-0.05}$	$-0.10\pm0.19^{\dagger}$
3C 287.1	0.2156	FR II	$+0.39^{+0.11}_{-0.12}$	$+0.52^{+0.14}_{-0.13}$	$-0.15^{+0.11}_{-0.11}$	$+0.30^{+0.06}_{-0.07}$
3C 289	0.9674	FR II	$+0.70^{+0.70}_{-0.80}$	$+0.42^{+0.50}_{-0.50}$	$-0.61^{+0.46}_{-0.39}$	$+0.64^{+0.28}_{-0.28}$
3C 292	0.7100	FR II	$+0.44^{+0.16}_{-0.16}$	$+0.56^{+0.15}_{-0.14}$	$+0.01^{+0.10}_{-0.10}$	$+0.21^{+0.07}_{-0.07}$
3C 293.1	0.7090	FR II	$+0.46^{+0.26}_{-0.28}$	$+0.83^{+0.26}_{-0.26}$	$+0.11^{+0.22}_{-0.21}$	$+0.31^{+0.14}_{-0.15}$
3C 300	0.2700	FR II	$+0.42^{+0.20}_{-0.20}$	$+0.62^{+0.22}_{-0.22}$	$+0.01^{+0.15}_{-0.14}$	$+0.23^{+0.11}_{-0.10}$
3C 306.1	0.4410	FR II	$+0.10^{+0.22}_{-0.21}$	$+0.45^{+0.23}_{-0.23}$	$-0.75^{+0.15}_{-0.14}$	$+0.51^{+0.11}_{-0.11}$
3C 315	0.1083	FR I	$+0.17^{+0.15}_{-0.15}$	$+0.09^{+0.17}_{-0.16}$	$-0.27^{+0.11}_{-0.10}$	$+0.20^{+0.08}_{-0.08}$
3C 319	0.1920	FR II	$+0.16^{+0.20}_{-0.20}$	$+0.51^{+0.23}_{-0.24}$	$-0.16^{+0.17}_{-0.16}$	$+0.24^{+0.11}_{-0.11}$
3C 323.1	0.2643	FR II	$+0.04^{+0.09}_{-0.08}$	$-0.15^{+0.10}_{-0.10}$	$-0.13^{+0.12}_{-0.12}$	$+0.02^{+0.06}_{-0.05}$
3C 327.1	0.4620	FR I	$-0.02^{+0.14}_{-0.14}$	$+0.49^{+0.17}_{-0.16}$	$-0.05^{+0.18}_{-0.18}$	$+0.12^{+0.09}_{-0.09}$
3C 332	0.1510	FR II	$+0.26^{+0.13}_{-0.13}$	$+0.55^{+0.11}_{-0.11}$	$+0.09^{+0.08}_{-0.08}$	$+0.14^{+0.06}_{-0.06}$
3C 336	0.9265	FR II	$-2.00^{+0.45}_{-0.00}$	$+2.00^{+0.00}_{-0.35}$	$-1.00^{+0.65}_{-0.45}$	$+0.59^{+0.37}_{-0.37}$
3C 340	0.7754	FR II	$+0.65^{+0.43}_{-0.43}$	$+1.25^{+0.29}_{-0.36}$	$-0.79^{+0.31}_{-0.26}$	$+0.84^{+0.20}_{-0.20}$
3C 341	0.4480	FR II	$-0.05^{+0.30}_{-0.30}$	$+0.73^{+0.32}_{-0.35}$	$-0.40^{+0.22}_{-0.20}$	$+0.34^{+0.15}_{-0.15}$
3C 352	0.8067	FR II	$+1.06^{+0.43}_{-0.47}$	$+0.94^{+0.37}_{-0.41}$	$+1.40^{+0.30}_{-0.42}$	$+0.26^{+0.26}_{-0.26}$
3C 357	0.1661	FR II	$+0.34^{+0.24}_{-0.22}$	$+0.92^{+0.21}_{-0.23}$	$-0.06^{+0.18}_{-0.17}$	$+0.34^{+0.12}_{-0.12}$
3C 381	0.1605	FR II	$+0.83^{+0.27}_{-0.30}$	$+0.70^{+0.37}_{-0.37}$	$-0.15^{+0.24}_{-0.22}$	$+0.43^{+0.17}_{-0.16}$
3C 382	0.0579	FR II	$+0.14\pm0.06^{\dagger}$	$+0.51\pm0.06^{\dagger}$	$-0.18\pm0.06^{\dagger}$	$+0.23\pm0.05^{\dagger}$
3C 388	0.0917	FR II	$-0.03^{+0.04}_{-0.04}$	$+0.08^{+0.04}_{-0.04}$	$-0.07^{+0.05}_{-0.05}$	$+0.04\pm0.05^{\dagger}$
3C 401	0.2011	FR II	$-0.25^{+0.05}_{-0.05}$	$-0.08^{+0.07}_{-0.07}$	$+0.15^{+0.09}_{-0.08}$	$-0.17^{+0.04}_{-0.04}$
3C 411	0.4670	FR II	$+0.14^{+0.19}_{-0.17}$	$-0.05^{+0.16}_{-0.16}$	$-0.05^{+0.17}_{-0.17}$	$+0.10^{+0.10}_{-0.10}$

Table 3. (*Continued...*)

Source	z	FR type	$R_{\rm soft}$	$R_{\rm medium}$	$R_{\rm hard}$	$R_{\rm broad}$
3C 424	0.1270	FR I	$-0.07^{+0.30}_{-0.30}$	$+0.61^{+0.31}_{-0.34}$	$-0.07^{+0.35}_{-0.35}$	$+0.35^{+0.20}_{-0.20}$
3C 427.1	0.5720	FR II	$+0.14^{+0.16}_{-0.16}$	$+0.39^{+0.16}_{-0.17}$	$-0.49^{+0.20}_{-0.19}$	$+0.33^{+0.10}_{-0.10}$
3C 432	1.7850	FR II	$+0.58^{+0.25}_{-0.25}$	$+0.13^{+0.28}_{-0.26}$	$+0.00^{+0.28}_{-0.26}$	$+0.37^{+0.15}_{-0.14}$
3C 434	0.3220	FR II	$-1.24^{+0.50}_{-0.37}$	$+0.45^{+0.65}_{-0.70}$	$-0.59^{+0.63}_{-0.54}$	$-0.12^{+0.41}_{-0.35}$
3C 435	0.4710	FR II	$+0.06^{+0.31}_{-0.29}$	$+0.70^{+0.37}_{-0.40}$	$-0.24^{+0.26}_{-0.25}$	$+0.26^{+0.18}_{-0.18}$
3C 436	0.2145	FR II	$+0.24^{+0.11}_{-0.11}$	$+0.16^{+0.11}_{-0.11}$	$+0.09^{+0.06}_{-0.06}$	$+0.01^{+0.05}_{-0.05}$
3C 438	0.2900	FR II	$-0.15^{+0.04}_{-0.04}$	$-0.12\pm0.05^{\dagger}$	$+0.06\pm0.05^{\dagger}$	$-0.10\pm0.05^{\dagger}$
3C 441	0.7080	FR II	$+0.38^{+0.47}_{-0.47}$	$+0.54^{+0.45}_{-0.49}$	$-0.77^{+0.32}_{-0.29}$	$+0.63^{+0.23}_{-0.23}$
3C 455	0.5430	FR II	$+0.46^{+0.27}_{-0.27}$	$+0.22^{+0.36}_{-0.36}$	$+0.21^{+0.25}_{-0.23}$	$+0.23^{+0.17}_{-0.16}$

†Approximation Equation (5) used for $S_{\rm ON}+S_{\rm OFF}>2000$.

C. SCIENCE APERTURE PROPERTIES, X-RAY AND RADIO OBSERVATION DATA.

Table 4 shows the properties of the science aperture and the X-ray and radio data used for each source. Table 5 shows the on-jet axis counts, off-jet axis counts, and the background level counts for the sources in our sample.

Table 4. Science aperture properties, X-ray and radio observation data.

Source	Quadrant[a] centroid	Position[b] angle (°)	Quadrant[c] radius (arcsec)	*Chandra*[d] obs. ID	Exposure time (ks)	Obs. date	Radio[e] obs freq. (GHz)
3C 16	0:37:45.367,+13:20:09.43	30.92	54.36	13879	11.92	2012-10-25	1.50
3C 19	0:40:55.056,+33:10:07.36	30.23	4.68	13880	11.90	2011-10-29	1.50
3C 20	0:43:09.171,+52:03:36.25	105.53	30.03	9294	7.93	2007-12-31	8.40
3C 22	0:50:56.220,+51:12:03.64	105.68	17.14	14994	9.35	2013-06-05	1.49
3C 29	0:57:34.897,-1:23:27.29	163.69	90.28	12721	7.95	2011-5-23	1.50
3C 34	1:10:18.540,+31:47:19.51	84.02	28.62	16046	11.92	2014-09-25	4.86
3C 42	1:28:30.103,+29:03:01.16	133.29	18.68	13872	11.92	2012-02-26	1.50
3C 46	1:35:28.506,+37:54:04.99	65.62	103.99	13881	11.92	2012-09-28	1.50
3C 52	1:48:28.909,+53:32:28.04	16.60	59.54	9296	8.02	2008-03-26	1.58
3C 54	1:55:30.285,+43:45:58.70	27.07	42.85	16049	11.92	2014-06-15	4.86
3C 55	1:57:10.558,+28:51:39.49	98.14	47.92	16050	11.92	2014-06-15	4.87
3C 79	3:10:00.102,+17:05:58.67	106.64	52.92	12723	7.69	2010-11-01	8.41
3C 129.1	4:50:06.648,+45:03:06.07	35.58	57.75	2219	9.63	2001-01-09	4.74
3C 133	5:02:58.470,+25:16:25.36	97.53	16.28	9300	8.03	2008-04-07	5.00
3C 135	5:14:08.350,+0:56:32.89	75.83	83.52	9301	7.93	2008-01-11	8.40
3C 166	6:45:24.098,+21:21:51.14	180.08	28.44	12727	7.95	2010-11-30	1.50
3C 169.1	6:51:14.801,+45:09:28.39	141.70	33.84	16056	11.92	2014-08-17	1.50
3C 171	6:55:14.746,+54:08:57.71	100.43	25.25	10303	59.46	2009-01-08	1.50

Table 4 *continued*

Table 4 *(continued)*

Source	Quadrant[a] centroid	Position[b] angle (°)	Quadrant[c] radius (arcsec)	*Chandra*[d] obs. ID	Exposure time (ks)	Obs. date	Radio[e] obs freq. (GHz)
3C 175.1	7:14:04.709,+14:36:22.80	71.51	7.20	15000	9.94	2013-02-10	5.00
3C 184.1	7:43:01.368,+80:26:25.86	157.78	111.60	9305	8.02	2008-03-27	1.50
3C 192	8:05:34.999,+24:09:50.30	124.38	112.10	9270	10.02	2007-12-18	8.40
3C 215	9:06:31.877,+16:46:11.89	149.10	34.84	3054	33.80	2003-01-02	4.86
3C 223.1	9:41:24.029,+39:44:42.04	14.21	43.20	9308	7.93	2008-01-16	8.40
3C 234	10:01:49.519,+28:47:08.64	61.58	69.71	12732	7.95	2011-01-19	1.50
3C 244.1	10:33:34.022,+58:14:35.36	166.90	32.99	13882	11.92	2013-01-16	1.50
3C 268.2	12:00:58.754,+31:33:21.34	22.02	56.50	13876	11.58	2012-07-07	1.50
3C 272	12:24:28.471,+42:06:35.89	22.25	48.71	16061	11.92	2015-03-01	1.50
3C 277	12:51:42.002,+50:34:24.99	73.82	94.81	16062	11.92	2015-03-03	1.50
3C 284	13:11:04.632,+27:28:07.31	99.95	133.24	12735	7.95	2010-11-17	1.50
3C 285	13:21:17.866,+42:35:15.17	76.23	110.24	6911	39.62	2006-06-18	1.42
3C 287.1	13:32:53.261,+2:00:45.68	92.56	79.20	9309	8.02	2008-03-23	1.50
3C 289	13:45:26.266,+49:46:32.79	109.53	6.87	15007	9.70	2013-07-28	8.44
3C 292	13:50:41.873,+64:29:35.88	164.74	88.25	16065, 17488	3.97, 7.97	2014-09-12, 2014-11-21	8.46
3C 293.1	13:54:40.999,+16:14:50.00	45.25	47.47	16066	11.92	2014-06-05	1.44
3C 300	14:22:59.861,+19:35:36.94	137.48	72.71	9311	7.94	2008-03-21	8.33
3C 306.1	14:55:01.409,-4:21:00.02	1.13	64.21	13885	11.92	2012-09-06	1.40
3C 315	15:13:40.068,+26:07:30.25	158.98	100.66	9315	7.67	2010-12-10	1.40
3C 319	15:24:05.028,+54:28:04.72	44.13	66.43	12737	8.44	2010-10-25	8.33
3C 323.1	15:47:43.518,+20:52:16.70	20.72	51.70	9314	7.93	2008-06-01	4.86
3C 327.1	16:04:45.408,+1:17:50.13	109.52	14.03	13887	11.11	2012-05-05	1.43
3C 332	16:17:42.552,+32:22:34.35	16.70	57.16	9315	7.93	2007-12-10	4.86
3C 336	16:24:39.084,+23:45:12.37	35.07	16.44	15008	2.00	2013-03-03	8.44
3C 340	16:29:36.588,+23:20:12.90	86.16	29.59	15010	9.95	2013-10-20	8.44
3C 341	16:28:03.994,+27:41:39.30	45.23	46.80	13888	11.64	2011-11-14	1.45
3C 352	17:10:44.126,+46:01:28.75	161.15	7.79	15013	9.95	2013-10-10	8.46
3C 357	17:28:20.105,+31:46:02.64	100.61	57.06	12738	7.95	2010-10-31	4.89
3C 381	18:33:46.313,+47:27:02.65	3.20	43.19	9317	8.06	2008-02-21	1.42
3C 382	18:35:03.389,+32:41:46.83	49.93	98.16	4910, 6151	54.15, 63.87	2004-10-27, 2004-10-30	8.46
3C388	18:44:02.378,+45:33:29.95	61.60	31.53	4756, 5295	7.37, 30.71	2004-01-09, 2004-01-29	1.39
3C 401	19:40:25.015,+60:41:36.00	25.50	14.19	3083, 4370	22.66, 24.85	2002-09-20, 2002-09-21	8.44
3C 411	20:22:08.455,+10:01:11.58	114.29	18.23	13889	11.92	2012-08-08	1.50
3C 424	20:48:12.101,+7:01:17.13	158.05	22.68	12743	7.95	2011-04-15	8.33
3C 427.1	21:04:06.924,+76:33:10.33	140.39	15.85	2194	39.45	2002-01-27	5.00
3C 432	21:22:46.333,+17:04:37.73	132.89	9.63	5624	19.78	2005-01-07	1.48
3C 434	21:23:16.241,+15:48:05.75	77.89	11.46	13878	11.92	2012-08-15	8.44

Table 4 *continued*

Table 4 *(continued)*

Source	Quadrant[a] centroid	Position[b] angle (°)	Quadrant[c] radius (arcsec)	*Chandra*[d] obs. ID	Exposure time (ks)	Obs. date	Radio[e] obs freq. (GHz)
3C 435	21:29:06.115,+7:32:54.96	54.38	28.69	13890	11.92	2012-08-14	1.50
3C 436	21:44:11.717,+28:10:19.47	174.45	62.99	9318, 12745	8.04, 7.95	2008-01-08, 2011-05-27	1.50
3C 438	21:55:52.255,+38:00:28.20	126.00	12.93	12879, 13218	72.04, 47.44	2011-01-30, 2011-01-28	1.50
3C 441	22:06:04.916,+29:29:19.98	147.48	24.46	14993, 15656	3.03, 6.98	2013-05-24, 2013-06-26	1.45
3C 455	22:55:03.888,+13:13:34.13	57.63	3.50	15014	9.95	2013-08-13	8.44

[a] Quadrant centroid position in RA and DEC (J2000).

[b] Position angle of the radio jet measured East of North in degrees.

[c] Quadrant radius in arcseconds.

[d] *Chandra* observation ID of the X-ray data.

[e] Frequency of the VLA radio observation.

Table 5. Science aperture ON, OFF, and B counts for the soft, medium, hard, and broad bands.

Source	Soft (0.5 − 1.2 keV)			Medium (1.2 − 2.0 keV)			Hard (2.0 − 7.0 keV)			Broad (0.5 − 7.0 keV)		
	ON	OFF	B	ON	OFF	B	ON	OFF	B	ON	OFF	B
3C 16	31	13	28	20	22	31	52	57	101	108	88	160
3C 19	11	14	1	12	8	1	3	4	1	26	24	3
3C 20	13	14	8	11	7	7	26	25	27	51	48	42
3C 22	10	2	2	9	3	3	10	15	7	33	15	13
3C 29	97	49	80	68	71	105	111	111	207	277	231	391
3C 34	14	8	10	14	17	8	15	25	20	58	40	39
3C 42	9	1	6	2	5	5	12	13	16	25	19	27
3C 46	83	85	105	64	77	114	218	204	362	353	378	581
3C 52	42	26	30	57	51	40	73	78	104	177	150	173
3C 54	10	9	13	19	8	22	39	48	56	78	55	90
3C 55	27	8	19	25	8	23	35	42	68	94	53	110
3C 79	27	22	23	25	23	22	51	57	77	111	96	122
3C 129.1	70	69	65	254	251	248	381	441	353	766	702	666
3C 133	6	5	2	8	9	4	12	22	9	40	28	14
3C 135	52	51	86	49	42	79	144	131	298	231	236	474
3C 166	21	11	5	25	13	9	16	22	26	67	40	41
3C 169.1	17	6	7	13	5	12	22	26	36	56	33	55
3C 171	65	56	44	51	38	58	123	110	159	228	219	261
3C 175.1	2	4	0	7	4	1	6	6	2	15	13	3
3C 184.1	81	65	123	77	61	130	233	225	344	384	360	596

Table 5 *continued*

Table 5 *(continued)*

Source	Soft (0.5 − 1.2 keV)			Medium (1.2 − 2.0 keV)			Hard (2.0 − 7.0 keV)			Broad (0.5 − 7.0 keV)		
	ON	OFF	*B*	ON	OFF	*B*	ON	OFF	*B*	ON	OFF	*B*
3C 192	154	103	123	111	93	164	277	303	552	568	472	839
3C 215	228	221	36	158	121	43	161	199	128	581	503	207
3C 223.1	14	11	19	19	12	16	39	45	58	79	60	93
3C 234	54	47	37	39	33	45	95	107	140	203	173	223
3C 244.1	26	17	15	22	17	11	25	37	36	83	60	62
3C 268.2	28	22	35	37	25	38	62	57	116	121	109	189
3C 272	15	6	21	18	15	15	38	44	66	77	59	103
3C 277	66	52	85	66	61	77	135	163	243	295	248	404
3C 284	108	81	145	87	104	169	241	274	497	484	410	811
3C 285	482	486	504	318	337	523	859	847	1661	1650	1686	2689
3C 287.1	124	88	58	102	64	63	143	162	190	391	301	311
3C 289	2	1	0	6	4	1	5	9	1	17	9	2
3C 292	83	57	109	90	55	93	182	181	311	357	298	514
3C 293.1	28	19	34	30	14	23	42	38	72	97	75	129
3C 300	50	35	67	43	25	64	87	86	170	180	148	301
3C 306.1	38	35	47	34	23	42	46	89	116	161	104	205
3C 315	75	65	78	68	63	115	144	181	310	324	273	503
3C 319	40	35	41	37	24	42	63	72	124	149	122	208
3C 323.1	175	168	31	112	129	28	110	123	75	424	417	134
3C 327.1	53	54	3	55	34	5	36	38	7	145	129	15
3C 332	90	71	31	129	77	38	234	215	96	433	382	164
3C 336	0	5	0	7	0	0	2	5	4	12	7	5
3C 340	9	5	7	14	4	9	12	24	22	47	22	38
3C 341	19	20	22	19	10	28	35	49	81	88	66	131
3C 352	6	2	1	8	3	0	9	2	3	19	15	4
3C 357	35	26	30	39	17	35	54	57	103	128	96	168
3C 381	23	11	24	15	8	21	32	36	60	75	52	104
3C 382	4280	4027	4388	5270	4389	6128	4742	5158	5319	8014	7234	8360
3C 388	743	765	31	834	772	33	497	530	58	2111	2030	122
3C 401	374	478	14	244	265	7	174	150	25	777	919	47
3C 411	37	32	2	43	45	4	43	45	12	130	119	19
3C 424	13	14	5	14	8	4	13	14	12	41	30	21
3C 427.1	50	44	9	49	34	8	29	45	22	144	106	39
3C 432	23	13	2	16	14	2	17	17	5	62	43	8
3C 434	2	7	3	3	2	1	3	5	7	10	11	11
3C 435	17	16	11	13	7	9	22	27	23	55	44	43
3C 436	164	134	221	154	135	236	574	532	972	848	844	1429

Table 5 *continued*

Table 5 *(continued)*

Source	Soft (0.5 − 1.2 keV)			Medium (1.2 − 2.0 keV)			Hard (2.0 − 7.0 keV)			Broad (0.5 − 7.0 keV)		
	ON	OFF	B	ON	OFF	B	ON	OFF	B	ON	OFF	B
3C 438	759	882	18	1236	1393	31	1328	1261	74	3264	3610	123
3C 441	7	5	5	8	5	5	10	20	21	35	20	31
3C 455	16	10	0	10	8	0	21	17	1	44	35	2

REFERENCES

Baum, S. A., Zirbel, E. L., & O'Dea, C. P. 1995, ApJ, 451, 88, doi: 10.1086/176202

Bennett, A. S. 1962, MmRAS, 68, 163

Blandford, R., Meier, D., & Readhead, A. 2019, ARA&A, 57, 467, doi: 10.1146/annurev-astro-081817-051948

Brandt, W. N., & Alexander, D. M. 2015, The Astronomy and Astrophysics Review, 23, doi: 10.1007/s00159-014-0081-z

Bridle, A. H. 1984, AJ, 89, 979, doi: 10.1086/113593

Buttiglione, S., Capetti, A., Celotti, A., et al. 2010, A&A, 509, A6, doi: 10.1051/0004-6361/200913290

Cavagnolo, K. W., McNamara, B. R., Nulsen, P. E. J., et al. 2010, ApJ, 720, 1066, doi: 10.1088/0004-637X/720/2/1066

Celotti, A., Ghisellini, G., & Chiaberge, M. 2001, MNRAS, 321, L1, doi: 10.1046/j.1365-8711.2001.04160.x

Croston, J. H., Hardcastle, M. J., Harris, D. E., et al. 2005, Astrophys. J., 626, 733, doi: 10.1086/430170

de Vries, M. N., Wise, M. W., Huppenkothen, D., et al. 2018, MNRAS, 478, 4010, doi: 10.1093/mnras/sty1232

Dunkley, J., Komatsu, E., R., N. M., et al. 2009, ApJS, 180, 306, doi: 10.1088/0067-0049/180/2/306

Edge, D. O., Shakeshaft, J. R., McAdam, W. B., Baldwin, J. E., & Archer, S. 1959, MmRAS, 68, 37

Fanaroff, B. L., & Riley, J. M. 1974, MNRAS, 167, 31P, doi: 10.1093/mnras/167.1.31P

Gehrels, D. 1986, ApJ, 303, 336

Hardcastle, M. J., & Croston, J. H. 2020, arXiv e-prints, arXiv:2003.06137. https://arxiv.org/abs/2003.06137

Hardcastle, M. J., Harris, D. E., Worrall, D. M., & Birkinshaw, M. 2004, ApJ, 612, 729, doi: 10.1086/422808

Harris, D., & Krawczynski, H. 2006, Annual Review of Astronomy and Astrophysics, 44, 463, doi: 10.1146/annurev.astro.44.051905.092446

Harris, D. E., Carilli, C. L., & Perley, R. A. 1994, Nature, 367, 713, doi: 10.1038/367713a0

Harris, D. E., Cheung, C. C., Biretta, J. A., et al. 2006, The Astrophysical Journal, 640, 211, doi: 10.1086/500081

Harris, D. E., & Krawczynski, H. 2002, ApJ, 565, 244, doi: 10.1086/324544

Heckman, T. M., & Best, P. N. 2014, Annual Review of Astronomy and Astrophysics, 52, 589–660, doi: 10.1146/annurev-astro-081913-035722

Hlavacek-Larrondo, J., Fabian, A. C., Edge, A. C. Ebeling, H., et al. 2012, MNRAS, 421, 1360, doi: 10.1111/j.1365-2966.2011.20405.x

Hoff, P. D. 2010, Springer Texts in Statistics: A First Course in Bayesian Statistical Methods (Springer), doi: 10.1007/978-0-387-92407-6

Ineson, J., Croston, J. H., Hardcastle, M. J., & Mingo, B. 2017, MNRAS, 467, 1586, doi: 10.1093/mnras/stx189

Jimenez-Gallardo, A., Massaro, F., Paggi, A., et al. 2021, ApJS, 252, 31, doi: 10.3847/1538-4365/abcecd

Joye, W. A., & Mandel, E. 2003, in Astronomical Society of the Pacific Conference Series, Vol. 295, Astronomical Data Analysis Software and Systems XII, ed. H. E. Payne, R. I. Jedrzejewski, & R. N. Hook, 489

Kharb, P., Lister, M. L., Marshall, H. L., & Hogan, B. S. 2012a, ApJ, 748, 81, doi: 10.1088/0004-637X/748/2/81

Kharb, P., O'Dea, C. P., Tilak, A., et al. 2012b, ApJ, 754, 1, doi: 10.1088/0004-637X/754/1/1

Ledlow, M. J., & Owen, F. N. 1996, The Astronomical Journal, 112, 9, doi: 10.1086/117985

Massaro, F., Harris, D. E., G., T., et al. 2013, ApJS, 206, 19, doi: 10.1088/0067-0049/206/1/7

Massaro, F., Tremblay, G. R., Harris, D. E., et al. 2012, ApJS, 203, 31, doi: 10.1088/0067-0049/203/2/31

Massaro, F., Harris, D. E., M., L. E. O., et al. 2015a, ApJS, 220, 5, doi: 10.1088/0067-0049/220/1/5

Massaro, F., Harris, D. E., Liuzzo, E., et al. 2015b, ApJS, 220, 5, doi: 10.1088/0067-0049/220/1/5

Massaro, F., Missaglia, V., Stuardi, C., et al. 2018, ApJS, 234, 7, doi: 10.3847/1538-4365/aa8e9d

McNamara, B. R., & Nulsen, P. E. J. 2007, Ann. Rev. Astron. Astrophys., 45, 117, doi: 10.1146/annurev.astro.45.051806.110625

Mingo, B., Hardcastle, J. M., Ineson, J. Mahatma, V., et al. 2017, MNRAS, 470, 2762, doi: 10.1093/mnras/stx1307

O'Sullivan, E., Giacintucci, S., David, L. P., et al. 2011, ApJ, 735, 11, doi: https://doi.org/10.1088/0004-637X/735/1/11

Padovani, P. 2016, The Astronomy and Astrophysics Review, 24, doi: 10.1007/s00159-016-0098-6

Padovani, P., Alexander, D. M., Assef, R. J., et al. 2017, The Astronomy and Astrophysics Review, 25, doi: 10.1007/s00159-017-0102-9

Park, T., Kashyap, V. L., Siemiginowska, A., et al. 2006, ApJ, 652, 610

Rafferty, D. A., McNamara, B. R., Nulsen, P. E. J., & Wise, M. W. 2006, ApJ, 652, 216, doi: 10.1086/507672

Sambruna, R. M., Gambill, J. K., Maraschi, L., et al. 2004, The Astrophysical Journal, 608, 698, doi: 10.1086/383124

Spinrad, H., Marr, J., Aguilar, L., & Djorgovski, S. 1985, Publications of the Astronomical Society of the Pacific, 97, 932, doi: 10.1086/131647

Stanley, E. C., Kharb, P., Lister, M. L., et al. 2015, ApJ, 807, 48, doi: 10.1088/0004-637X/807/1/48

Tadhunter, C. 2016, The Astronomy and Astrophysics Review, 24, doi: 10.1007/s00159-016-0094-x

Tavecchio, F., Maraschi, L., Sambruna, R. M., & Urry, C. M. 2000, ApJL, 544, L23. http://stacks.iop.org/1538-4357/544/i=1/a=L23

van Dyk, D. A., Connors, A., Kashyap, V. L., & Siemiginowska, A. 2001, ApJ, 548, 224

Weisskopf, M. C., Brinkman, B., Canizares, C., et al. 2002, Publications of the Astronomical Society of the Pacific, 114, 1, doi: 10.1086/338108

Worrall, D. M. 2009, A&A Rv, 17, 1, doi: 10.1007/s00159-008-0016-7